

Article

System for Analysis of Wind Collocations (SAWC): A Novel Archive and Collocation Software Application for the Intercomparison of Winds from Multiple Observing Platforms

Katherine E. Lukens^{1,2,*}, Kevin Garrett³, Kayo Ide⁴, David Santek⁵, Brett Hoover⁶, David Huber⁷, Ross N. Hoffman^{1,2} and Hui Liu^{1,2}

¹ NOAA/NESDIS/Center for Satellite Applications and Research (STAR), College Park, MD 20740, USA; ross.n.hoffman@noaa.gov (R.N.H.); hui.liu@noaa.gov (H.L.)

² Cooperative Institute for Satellite Earth System Studies (CISESS), University of Maryland, College Park, MD 20740, USA

³ NOAA/NWS/Office of Science and Technology Integration (OSTI), Silver Spring, MD 20910, USA

⁴ University of Maryland, College Park, MD 20742, USA

⁵ Cooperative Institute for Meteorological Satellite Studies (CIMSS), University of Wisconsin-Madison (UW-Madison), Madison, WI 53706, USA; dave.santek@ssec.wisc.edu

⁶ Lynker Technologies, NOAA/NWS/NCEP/Environmental Modeling Center (EMC), College Park, MD 20740, USA

⁷ Redline Performance Solutions, LLC, NOAA/NWS/NCEP/Environmental Modeling Center (EMC), College Park, MD 20740, USA

* Correspondence: katherine.lukens@noaa.gov



Citation: Lukens, K.E.; Garrett, K.; Ide, K.; Santek, D.; Hoover, B.; Huber, D.; Hoffman, R.N.; Liu, H. System for Analysis of Wind Collocations (SAWC): A Novel Archive and Collocation Software Application for the Intercomparison of Winds from Multiple Observing Platforms. *Meteorology* **2024**, *3*, 114–140. <https://doi.org/10.3390/meteorology3010006>

Academic Editors: Edoardo Bucchignani and Paul D. Williams

Received: 4 November 2023

Revised: 20 February 2024

Accepted: 29 February 2024

Published: 7 March 2024



Copyright: © 2024 by the authors. Licensee MDPI, Basel, Switzerland. This article is an open access article distributed under the terms and conditions of the Creative Commons Attribution (CC BY) license (<https://creativecommons.org/licenses/by/4.0/>).

Abstract: Accurate atmospheric 3D wind observations are one of the top priorities for the global scientific community. To address this requirement, and to support researchers' needs to acquire and analyze wind data from multiple sources, the System for Analysis of Wind Collocations (SAWC) was jointly developed by NOAA/NESDIS/STAR, UMD/ESSIC/CISESS, and UW-Madison/CIMSS. SAWC encompasses the following: a multi-year archive of global 3D winds observed by Aeolus, sondes, aircraft, stratospheric superpressure balloons, and satellite-derived atmospheric motion vectors, archived and uniformly formatted in netCDF for public consumption; identified pairings between select datasets collocated in space and time; and a downloadable software application developed for users to interactively collocate and statistically compare wind observations based on their research needs. The utility of SAWC is demonstrated by conducting a one-year (September 2019–August 2020) evaluation of Aeolus level-2B (L2B) winds (Baseline 11 L2B processor version). Observations from four archived conventional wind datasets are collocated with Aeolus. The recommended quality controls are applied. Wind comparisons are assessed using the SAWC collocation application. Comparison statistics are stratified by season, geographic region, and Aeolus observing mode. The results highlight the value of SAWC's capabilities, from product validation through intercomparison studies to the evaluation of data usage in applications and advances in the global Earth observing architecture.

Keywords: SAWC; collocation; wind; Aeolus; aircraft; AMV; Loon; sonde

1. Introduction

In 2018, the National Academies Press released the 2017–2027 decadal survey, which listed accurate 3D wind observations as a top priority for the Earth science community [1], where 3D indicates that the observed winds are spread over all three geometric dimensions, although the observations are actually two-dimensional (2D) horizontal winds. Wind observations have a critical impact on weather forecasting, data assimilation (DA), ocean currents, wildfires, air quality, the energy sector, the spread of disease, and other applications. For decades, winds have been observed in situ by commercial aircraft, sondes (e.g., rawin- and dropsondes), and near-space superpressure balloons [2–5], and by satellites.

Satellite winds include atmospheric motion vectors (AMVs) that are derived by tracking moisture and water vapor (WV) features in satellite imagery through time (e.g., [6–9]), and Doppler wind lidar winds, such as those observed by the Atmospheric Laser Doppler Instrument (ALADIN) onboard the Aeolus satellite [10,11].

Numerous studies have been conducted to address the decadal survey's 3D wind requirement (e.g., [7,8,12–26]). Many involve the characterization and validation of AMVs, e.g., from establishing collocation standards between sondes and AMVs (time difference < 90 min, height difference < 25 hPa, horizontal distance < 150 km) [12] to investigating the importance of the AMV error characteristics (e.g., height assignment accuracy and spatial error correlations) for DA [14,15], as well as intercomparing AMVs derived by several international satellite wind producing centers [7,8,16,19]. Recent studies now include Aeolus in their comparisons, e.g., to validate Aeolus winds [20,23], and to leverage Aeolus as a potential comparison standard for AMV characterization [24,25].

The results from these different studies are not easily comparable, due in part to each study using widely varying collocation criteria. As there are few accepted collocation standards for different wind pairings in the literature and broader wind community, researchers often find the need to create their own criteria and algorithms. The standards that do exist were developed decades ago, yet are still used today, i.e., those for sondes versus AMV comparisons [12]. It has been recommended that such standards be reassessed to account for today's advanced imagers [27]. Furthermore, it is often necessary for researchers to acquire and reformat disparate data from numerous sources and develop their own analysis tools in order to achieve specific project objectives. These steps can be time consuming and can delay progress, particularly for projects assigned short periods of performance.

To support researchers' needs to acquire and analyze wind data from multiple sources, and to further address the 3D wind requirement, the System for Analysis of Wind Collocations (SAWC) was jointly developed by the NOAA National Environmental Satellite, Data, and Information Service (NESDIS) Center for Satellite Applications and Research (STAR), the Cooperative Institute for Satellite Earth System Studies (CISESS) at the University of Maryland, and the Cooperative Institute for Meteorological Satellite Studies (CIMSS) at the University of Wisconsin-Madison. SAWC is unique in that it provides the data and tools that one needs for wind observation research all in one place, as follows: a multi-year, public archive of global 3D winds that have been acquired from multiple observing platforms and converted to a common format (netCDF); identified pairings between select datasets also available in netCDF; and a downloadable software application developed for users to interactively collocate wind observations and visually and statistically compare them based on their research needs. The capability of SAWC is wide-ranging, from product validation through intercomparison studies to the evaluation of data usage in applications and advancements in the global Earth observing architecture.

This article introduces SAWC and its components, including the collocation application and a multi-year collection of wind observations from Aeolus, satellite imagery (AMVs), aircraft, sondes, and Loon stratospheric superpressure balloons [5]. Examples of SAWC's utility are presented here, including a one-year quantitative evaluation of the Aeolus level 2B (L2B) winds (Baseline 11 L2B processor version) compared to four conventional wind datasets and an example assessment of observation error estimates in DA.

Section 2 provides an overview of SAWC and its components. Section 3 discusses example applications of SAWC. Section 4 presents a summary and conclusions.

2. Overview of SAWC

SAWC encompasses a global wind data archive (see Section 2.1), identified pairings between selected datasets in the form of index files (see Section 2.2.1), a collocation software application consisting of a collocation tool (see Section 2.2.1) and a plotting tool (see Section 2.2.2), and a user manual [28]. All of the components of SAWC are hosted and maintained on the NOAA/NESDIS/STAR public server, are continuously updated, and are publicly available online, as follows:

- SAWC Website: <https://www.star.nesdis.noaa.gov/sawc> (accessed on 28 February 2024).
- Data Home: <https://www.star.nesdis.noaa.gov/data/sawc> (accessed on 28 February 2024).
- Wind Archive: https://www.star.nesdis.noaa.gov/data/sawc/wind_datasets (accessed on 28 February 2024).
- Collocation Software Application and Index Files: <https://www.star.nesdis.noaa.gov/data/sawc/collocation> (accessed on 28 February 2024).
- User Manual: https://www.star.nesdis.noaa.gov/data/sawc/User_Manual (accessed on 28 February 2024).

SAWC’s end-to-end process comprises the following three main steps: (1) data acquisition, (2) collocation of winds, and (3) analysis and visualization (Figure 1). In Step (1), data are acquired from various sources, reformatted to a common format (netCDF), and archived for public dissemination (hereafter, source data files). Note that the user does not interface with Step (1), rather, the data files are archived in netCDF and are then made available to the user.

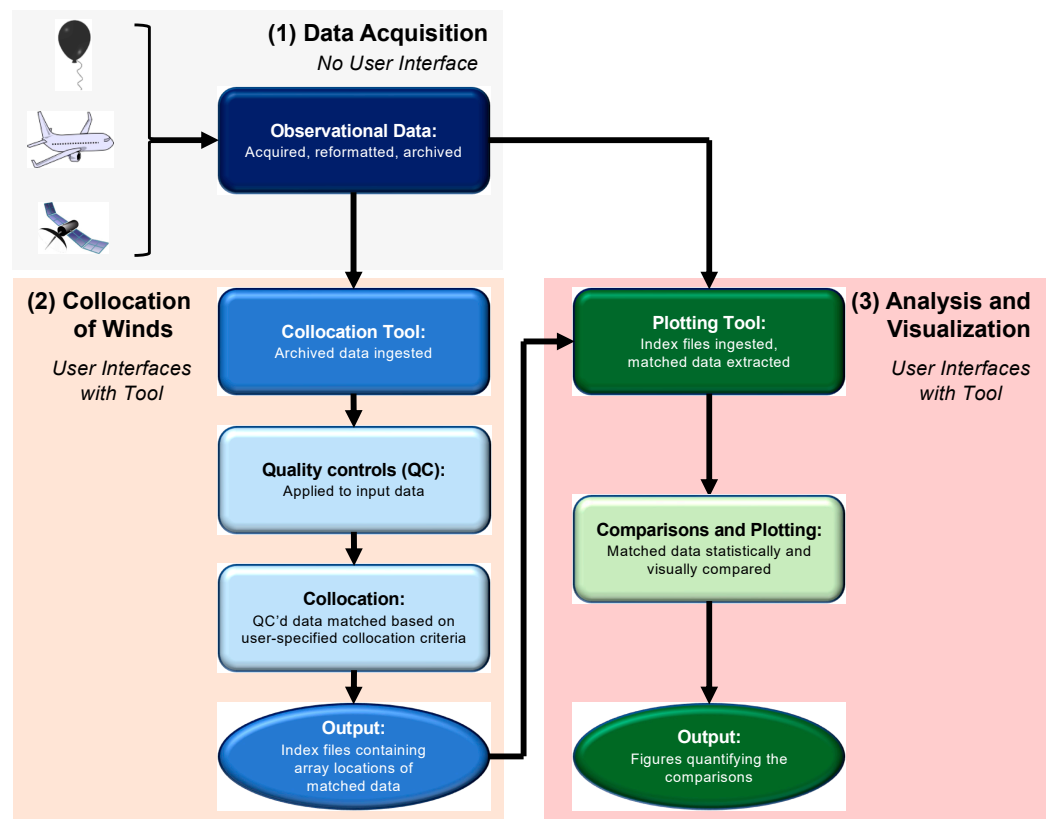


Figure 1. Flow chart illustrating SAWC’s end-to-end process. Note that the user interfaces with the collocation and plotting tools in Steps (2) and (3), respectively.

The user interface with SAWC occurs during Steps (2) and (3) by setting adjustable parameters in configuration files. In Step (2), the application’s collocation tool is used to ingest and match winds from user-selected source data and generate index files, i.e., netCDF files that contain arrays of indices or locations of the matched winds in the source data files. In Step (3), the application’s plotting tool uses these index files to extract and compare the matched winds through visual and statistical analysis. A host of figures are generated that quantify the comparisons. See Section 2.2 for more on the collocation application.

2.1. Datasets Available

At the time of writing, several global wind observation datasets have been acquired and archived. These include Doppler wind lidar (DWL) observations from Aeolus, satellite-derived winds (i.e., AMVs), and in situ upper-level winds observed by sondes, stratospheric

superpressure balloons, and aircraft. These datasets are included in the SAWC archive as a first step; moreover, SAWC can be expanded to include others such as surface, radial, and profiler winds, which have yet to be included as they are out of the scope of the wind comparison study presented in Section 3. Table 1 lists the file formats and temporal coverage of the archived winds currently available in SAWC, as well as a few key variables provided in each dataset. The typical spatial distributions are shown in Supplemental Material Figure S1.

Table 1. Source wind datasets currently available in SAWC. The file formats, temporal coverage, vertical coordinates, and wind representation variables available per dataset are listed. Additionally, all datasets include time variables (year, month, day, and hour) as well as horizontal coordinates (latitude and longitude). The file formats are the Network Common Data Form (netCDF), the Binary Universal Form for the Representation (BUFR) of meteorological data, and the ESA Earth Explorer (EE) format.

Wind Datasets	SAWC File Formats	Temporal Coverage	Vertical Coordinates	Wind Representation
Aeolus	netCDF; BUFR; EE	September 2018–April 2023	Height; Pressure	HLOS Wind Velocity; Azimuth Angle
Loon	netCDF-4	2011–2021	Height; Pressure	u-/v-components; Wind Direction
Sonde	netCDF-4	September 2018–Present Day	Height; Pressure	Wind Speed; Wind Direction
Aircraft	netCDF-4	September 2018–Present Day	Height	Wind Speed; Wind Direction
AMV	netCDF-4	September 2018–Present Day	Pressure	Wind Speed; Wind Direction

Different observing systems use different physical measurement techniques to derive wind information. In situ measurements, including balloons and aircraft, derive winds from the sequence of global positioning system (GPS)-measured locations. AMVs are based on tracking features identified in imagery. Active wind measurement systems measure the Doppler frequency shifts of reflected lidar or radar signals. Note that active measurement provides one component of the wind vector for each viewing geometry.

The different measurement techniques are subject to different observing and retrieval errors, and the different space–time volumes sampled are associated with different representativeness errors, since scales averaged over by one observing system are observed by a second observing system. For the in situ systems, the wind is representative of a short segment of the path of the balloon or aircraft. For active systems, the wind is representative of the volume defined by the temporal range gates and by the aperture and the scanning or transit strategy of the telescope. For AMVs, the space–time volume is not well-defined and, in particular, the vertical assignment of the AMVs introduces correlated errors. AMVs are mostly single-level wind observations, since they are based on tracking features in imagery. The exception to this is for WV clear sky (WVclear) AMVs, which are based on tracking features in retrieved WV imagery. When SAWC collocates two observing systems, the differences are due to measurement and representativeness errors, as well as to collocation errors, since the locations and times are not perfectly matched. The Aeolus vs. point measurement representativeness error can be estimated by using high-resolution model output [23].

In the upper troposphere, when wind shear is high, comparison of the 1.5 to 2 km Aeolus Rayleigh-clear vertical resolution to a point measurement can introduce substantial differences. If the point measurement is a profile, like a sonde, it can be averaged appropriately, but nothing can be done for aircraft or balloons cruising at a more or less constant altitude. We note that SAWC performs no special averaging of this type. Although Aeolus data have been found to be very helpful in data assimilation in this situation [29], it has also

been suggested that a realistic observation operator that averages the model winds over the Aeolus measurement volume would improve the assimilation of Aeolus winds [30].

The Aeolus L2B winds were produced by the European Space Agency (ESA) and the European Centre for Medium-Range Weather Forecasts (ECMWF) [31,32]. Aeolus winds were observed by the DWL onboard the Aeolus satellite that traveled on a dawn/dusk orbit during 2018–2023. The Aeolus lidar was aimed to the right of the spacecraft so that horizontal line-of-sight (HLOS) winds were observed from 0 to 30 km altitude in a plane that intersects the Earth's surface 230 km to the right of the sub-satellite track, with an incidence angle of about 37.6° [33]. Two main wind regimes were retrieved for use in research and operations, as follows: Rayleigh-clear winds were derived from molecular backscattering and represented winds in clear scenes, and Mie-cloudy winds were derived from aerosol and cloud particle backscattering and represented winds in cloudy scenes. The processing algorithms can vary both the horizontal resolution, by adjusting the averaging time, and the vertical resolution, by adjusting the range-bin settings [34]. Normally, and in this study, the Rayleigh-clear winds are retrieved every 90 km horizontally in 1–2 km vertical bins, and the Mie-cloudy winds are retrieved every 15 km horizontally in 0.5–1.0 km vertical bins. Note that the data quality changes over the course of Aeolus' lifetime due to the DWL signal loss [35] and because the L2B processor was upgraded several times. For this study, the processor version is Baseline 11 and the Aeolus wind datasets are referred to as L2B11. The typical spatial coverage of Aeolus for a 24-h period is displayed in Figure S1a.

The AMV, aircraft, and sonde winds are provided by the National Centers for Environmental Prediction (NCEP) and are processed by the NCEP Environmental Modeling Center (EMC) Observations Processing (ObsProc) team prior to their conversion to netCDF and archival in SAWC. Aircraft winds are observed at flight level in the upper troposphere/lower stratosphere and in the ascending and descending legs of each flight. The spatial coverage is regional and dependent upon commercial flight paths. An example of the daily coverage of aircraft observations is shown in Figure S1b. Sondes take direct in situ wind observations as they ascend through the atmosphere from the surface to the upper troposphere/lower stratosphere. The spatial coverage is sparse and mostly over land (Figure S1c). Note that all of the SAWC-archived winds from aircraft, satellite imagery, and sondes contain only unrestricted observations.

All of the available AMVs are archived and are from both geostationary (GEO) and polar Earth-orbiting (LEO) satellites. The AMVs include infrared (IR), visible, WVclear, and WV cloudy-sky (WVcloud) AMVs. IR AMVs include both short- and long-wave IR AMVs. WVclear and WVcloud AMVs are also known as WV deep-layer and WV cloud-top AMVs, respectively. These AMVs are all single-level observations at the cloud top with the exception that WVclear AMVs are generated at multiple levels by tracking features in WV fields retrieved under clear conditions. The spatial coverage for the entire dataset is near-global (Figure S1d), with partial gaps at around 60° S and 60° N. These gaps are present because viewing angles of 60° or more are too extreme for reliable imaging from GEO, and LEO AMVs depend on at least two close-in-time but separate overpasses, which only occur close to the poles.

The stratospheric superpressure balloon observations were provided by Loon, a former subsidiary of Google's parent company, Alphabet (Mountain View, CA, USA). From 2011 to 2021, Loon deployed a network of these tennis-court-sized balloons, each carrying an instrument payload platform used to provide Internet connectivity to regions with limited access. The balloon configurations were specifically designed to withstand harsh stratospheric conditions for months at a time. A ground team was able to control their movements by remotely adjusting the balloon pressure, allowing the configurations to move into different airstreams. In situ atmospheric observations were reported at balloon level (~ 50 – 100 hPa or 18–20 km) at a frequency of ~ 1 – 20 min. The spatial coverage was regional (Figure S1e) and varied on a time scale of months to years as the Loon mission objectives varied.

All of the datasets span the entire lifetime of Aeolus (September 2018–April 2023), except for the acquisition of AMVs, aircraft, and sonde winds, which continues beyond Aeolus' lifetime to the present day, and the Loon record, which ran from 2011 to 2021, when the Loon project ended (see Table 1). All of the netCDF files contain 6 h of data centered around four numerical weather prediction (NWP) analysis times (00, 06, 12, and 18 UTC), except for the Aeolus netCDF files, which cover 24-h periods (00:00–23:59 UTC), with separate files for each Aeolus wind regime. The archived Aeolus data are also available in ECMWF BUFR and ESA's Earth Explorer (EE) formats.

2.2. Collocation Software Application

Unique collocation techniques were developed at CIMSS [18] and incorporated into the SAWC collocation application, a Python-based software package developed to match winds from different datasets based on user-specified criteria. There are two main tools that make up the collocation application: a collocation tool and a plotting tool. The collocation tool matches wind observations from different datasets and only considers the time and 3D locations of the wind observations, and not the wind speed or direction. The plotting tool intercompares the matched wind observations, performs statistical analyses, and generates plots quantifying the comparisons. Key SAWC details are given in the tables of Appendix A, and a complete description of SAWC is given in the SAWC user manual [28]. The SAWC management components include index files and the collocation and plotting software application package (Table A1). The index files in the netCDF-4 format cover select temporal periods and include the indices of the matched winds along with the differences in time, height/pressure, and distance for each pair of matched winds.

2.2.1. Collocation Tool

To collocate the winds, the user modifies various input parameters for the collocation tool. Table A2 lists the main input parameters that the user can change; in addition, a complete list is provided in the SAWC user manual [28]. The main input parameters define the datasets to be processed (date range, dataset names, and Aeolus dataset type), where the output dataset is stored (path to output index file), and the options controlling the collocation (collocation criteria and number of matches allowed) and quality controls (QCs) (quality control flags, AMV quality indicator, and AMV quality indicator option).

Prior to collocation, QCs are applied to the input wind observations if the user chooses this option. At present, QCs are readily available for two datasets, Aeolus and AMVs, based on the recommendations from the data producers and the broader wind community (Table A3). The default QCs in SAWC, which are applied in this study, include the following:

- Aeolus winds must be at pressures less than 800 hPa. Thus, all Aeolus boundary layer winds are rejected.
- Aeolus winds and AMVs must be high quality, as estimated by the data producers. For Aeolus, the L2B uncertainty must be small. For AMVs, the quality indicator (QI) must be at least 80.

It is important to note that the user is able to change the QC parameters and/or add QCs for the other datasets if desired.

After QC, a 4D collocation (latitude, longitude, height/pressure, and time) is performed between the "Driver" dataset and one or more "Dependent" datasets, where the Driver is the dataset with which all Dependent datasets are collocated. The following four collocation criteria are needed per Dependent dataset: the maximum time difference in minutes, the maximum collocation distance in km, the maximum log₁₀ (pressure) difference in log₁₀ (hPa), and the maximum height difference in km. The default settings are 60 min, 100 km, 0.04 log₁₀ (hPa), and 1 km, respectively, for all datasets, except for collocations involving sondes, where the first two criteria are relaxed to 90 min and 150 km, respectively (Table A4). The input parameters allow users to override these default settings if desired.

During the collocation process, all Dependent observations are compared to each Driver observation. This means that one Dependent observation may be collocated with multiple Driver observations, or one Driver observation may be collocated with multiple Dependent observations. If a Dependent observation meets all of the selected collocation criteria, the Driver and Dependent array locations (i.e., indices) in the respective source data files are saved to the output index file for that Driver–Dependent pairing. The index files for selected pairs of datasets and time periods are available in the SAWC archive. By saving the matched indices and not a copy of the collocated data, disk space is saved. In addition, each index file contains the actual distances and differences in time and height/pressure between each pair of collocated winds. The index files can be subsetted with stricter, but not looser, collocation criteria.

2.2.2. Plotting Tool

The application's plotting tool consists of visualization and statistical analysis functions developed for use in conjunction with the SAWC wind archive. The plotting tool uses the index files generated by the collocation tool to extract and compare matched wind data. The user can modify several parameters that control the actions of the plotting tool (Table A5), including the parameters that define the datasets to be processed (start date, end date, Driver dataset name, and Dependent dataset names), where the index dataset and plots are to be stored (path to input index files and path to output plots), and to set the option to super-ob the matches (super-ob choice). In the context of SAWC, super-obbing refers to the averaging of all Dependent winds (from one Dependent dataset, e.g., all aircraft winds) that match the same Driver observation, resulting in one Dependent observation (representing the mean of the multiple collocations) per one Driver observation. Super-obbing is recommended to reduce processing time and produce smoother results. Super-obbing produces smoother results because smaller scales are averaged over, reducing representativeness error. However, this effect is not uniform, since the number of Dependent observations may vary from one Driver location to another.

After the HLOS conversion (if applicable), a second set of QCs is applied to all winds. This entails a general wind gross check, where wind differences between the Driver and the Dependent observations are rejected if they exceed $|25|$ m/s. This threshold was chosen to omit extraneous outliers and follows other established collocation practices (e.g., [36]). In the future, SAWC may implement a more selective outlier check based on the z-score (e.g., [37]) that could account for the space–time variations in error statistics. The gross check is applied to all dataset pairings selected for comparison, after which the plotting tool analyzes the QC'd and matched winds and generates a host of figures that quantify the comparisons. The plotting tool computes global and regional statistics simultaneously, where regional refers to the Northern Hemisphere extratropics (NH), Tropics (TR), and Southern Hemisphere extratropics (SH), and the region borders are 30° N and 30° S. Seasonal statistics may be computed by rerunning the plotting tool for different date ranges. In addition, the plotting tool must be run separately for each Aeolus wind regime (Rayleigh-clear or Mie-cloudy). In the figures and in the text of the next section, we refer to these two wind regimes as RayClear and MieCloud.

The collocation and plotting tools are designed to be flexible and to handle additional datasets not yet available in the archive. The user manual provides instructions on how to include such datasets for offline comparisons [28].

3. Demonstrations of SAWC's Utility

3.1. Comparisons between Wind Datasets

This section exemplifies the value of SAWC through a one-year global evaluation of Aeolus RayClear and MieCloud winds. Other wind datasets are compared to the Aeolus winds. The Aeolus data are an ideal basis of comparison in terms of their uniform global coverage. However, other attributes of the Aeolus data are less than ideal. First, Aeolus only observes HLOS winds. HLOS winds do have both a speed and direction, but the direction is constrained to be along the HLOS, and both are represented in SAWC by a signed speed

with positive values directed away from the satellite. Therefore, the non-Aeolus winds in any comparison must be first projected onto the Aeolus HLOS direction (see Appendix B). The alternative of converting the Aeolus HLOS winds to full vector winds by assuming, for example, knowledge of the wind direction from an analysis dataset, is not useful, since the results would be a combination of two datasets. There are also known biases in the Aeolus winds that might make these data less than ideal as a comparison standard. However, these have largely been eliminated by procedures for calibration [38] and for corrections, including the Rayleigh–Brillouin correction [39], the telescope temperature correction [40,41], and the dark current correction [42].

Figure 2 shows the mapped number densities or counts per grid cell of QC'd Aeolus winds for the study period (00 UTC 1 September 2019 through 18 UTC 31 August 2020) prior to collocation. Aeolus winds are observed on a global scale from the surface to 30 km. Higher MieCloud number densities highlight cloudy regions, while the number density for RayClear winds presents a more uniform distribution globally. For example, the MieCloud numbers are less in the subtropical ocean areas (Figure 2c) and in the stratosphere (Figure 2d). The MieCloud numbers are greater in the Antarctic stratosphere than in the Arctic stratosphere, which is consistent with the greater prevalence of polar stratospheric clouds in the Antarctic ([43], their Figure 17). In Figure 2a,c there are some faint linear features that correspond to orbits with no observations, due to the special instrument calibration modes required for the pixel-wise dark signal correction of the Aeolus winds [42]. The one-year evaluation is stratified by season (September–October–November (SON), December–January–February (DJF), March–April–May (MAM), and June–July–August (JJA)), geographic region (NH, TR, and SH), and Aeolus wind regime (RayClear and MieCloud).

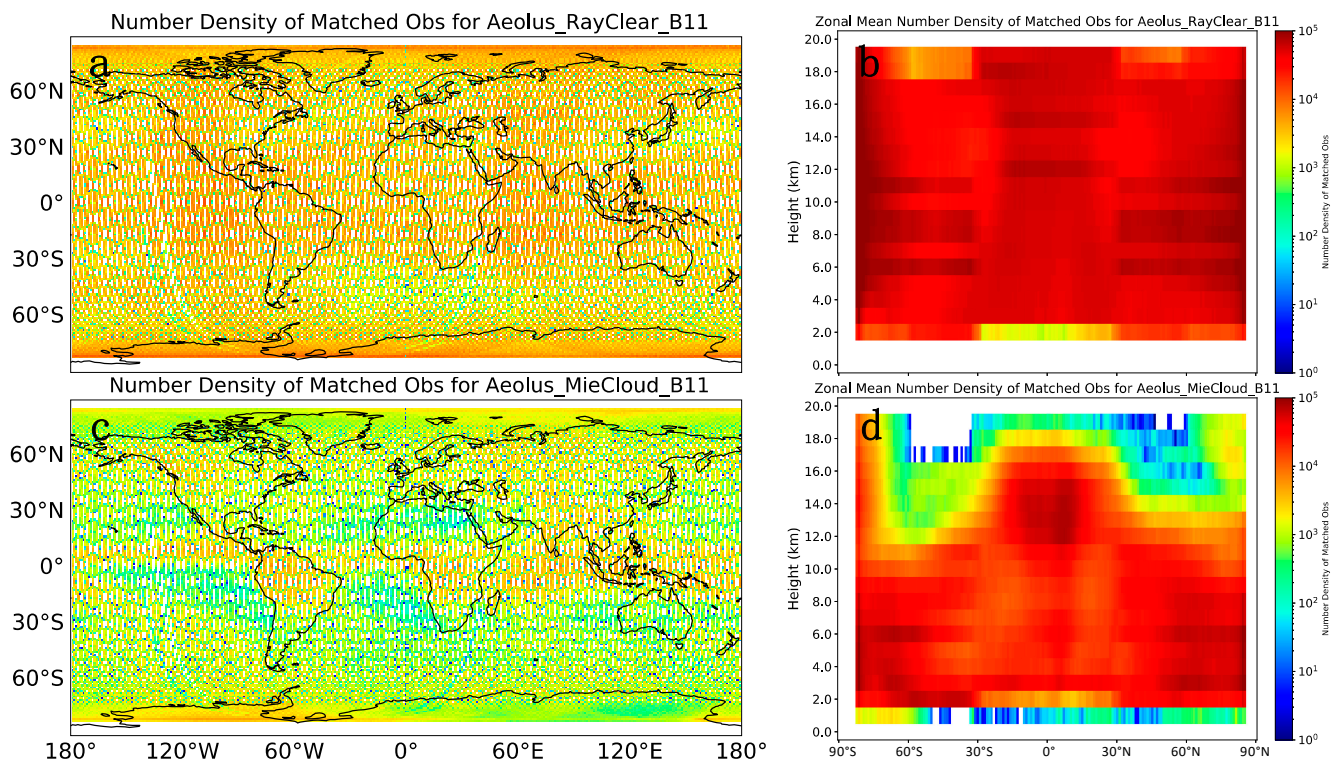


Figure 2. Observation number density maps on a latitude–longitude plane (left, (a,c)) and height–latitude plane (right, (b,d)) for QC'd Aeolus winds from the (a,b) Rayleigh-clear regime and (c,d) Miecloudy regime for September 2019–August 2020, prior to collocation with the Dependent datasets. The colors indicate the number density per grid cell, with dimensions of 1° × 1° for panels (a,c) and 1 km × 1° for panels (b,d).

For the demonstration, the Driver dataset is Aeolus, and the Dependent datasets contain aircraft, sondes, Loon stratospheric balloons, and AMV wind observations. The winds are QC'd using the wind community-recommended parameters listed in Table A3, and the Dependent observations are collocated with the Driver observations using the default collocation criteria listed in Table A4. Prior to the analysis, the collocated Dependent winds are projected onto the Aeolus HLOS direction and are super-obbed for every Driver observation. The general wind gross check (see Section 2.2.2) is applied to all collocated pairs.

Statistics are computed for the collocation samples and include correlation (r) and root mean square differences (RMSDs), as defined in [44], as well as the mean differences in wind speed (Mean_Diffs) and standard deviations (SD) of those differences (SD_Diffs), as defined in [25] (notated in [25] as MCD and SDCD, respectively). The SD_Diffs and RMSDs tend to be very similar and, as such, any discussion involving SD_Diffs also applies to the RMSDs. In addition, the statistical significance of wind differences at the 95% confidence level (p -value < 0.05) is assessed using the paired two-tailed Student's t -test.

3.1.1. Dataset Comparison Results

Figure 3 presents the number densities of collocated observation pairs between Dependent and Aeolus RayClear winds. The distributions of the collocation pairs are truly 3D. The right and left columns of the panels show map views and zonal cross sections, respectively. Figure 3a shows that aircraft winds matched with Aeolus cover much of the NH, with pockets of higher densities observed over the contiguous United States and Europe, as expected, (e.g., [45], their Figure 5a). There are few collocations over the SH, largely due to sparse spatial coverage of aircraft in the region, particularly over the oceans. Many aircraft winds are matched with Aeolus at cruise altitude (8–12 km) in the upper troposphere (Figure 3b) and also in the mid- and lower troposphere in the ascending and descending legs of each flight.

AMVs exhibit near-global coverage (Figure 3c) and are collocated with Aeolus throughout the vertical (800–100 hPa) (Figure 3d). The absence of collocations below 800 hPa is due to the QC criteria adopted for Aeolus winds (see Section 2.2.1). There is a noticeable dip in numbers near 65 degrees of latitude between the regions of excellent coverage for GEO and LEO observing systems. The gap in AMVs over the western Pacific region near 120° E occurs because (for unknown reasons) certain Himawari-8 UTC times are never archived in the NOAA database. Sonde winds are generally collocated with Aeolus over land, particularly in the NH, again, throughout the vertical (Figure 3e,f). Note the horizontal bars of lower number density displayed in Figure 3d,f. There are some 25 hPa bins that are rarely sampled. This is a result of collocating Dependent winds with Aeolus at Aeolus pressure levels rather than heights. Aeolus winds are each assigned both a height and a pressure value, but because they are vertically sampled based on height, and height is linear in the vertical, while pressure is nonlinear. Aeolus winds have a more uniform distribution of number density on a height–latitude plane relative to a pressure–latitude plane.

Loon winds are collocated with Aeolus in the lower stratosphere in the TR and part of the SH (Figure 3g,h) during the collocation period. Note that the 3D distribution of Loon matches may vary depending on the time period chosen. Aeolus MieCloud collocations exhibit similar spatial distributions (Figure S2); however, aircraft and sondes total somewhat fewer collocations, and AMVs have more collocations than their RayClear counterparts. Additionally, there are no collocations between MieCloud and Loon, as Loon observes winds at levels above the MieCloud observations.

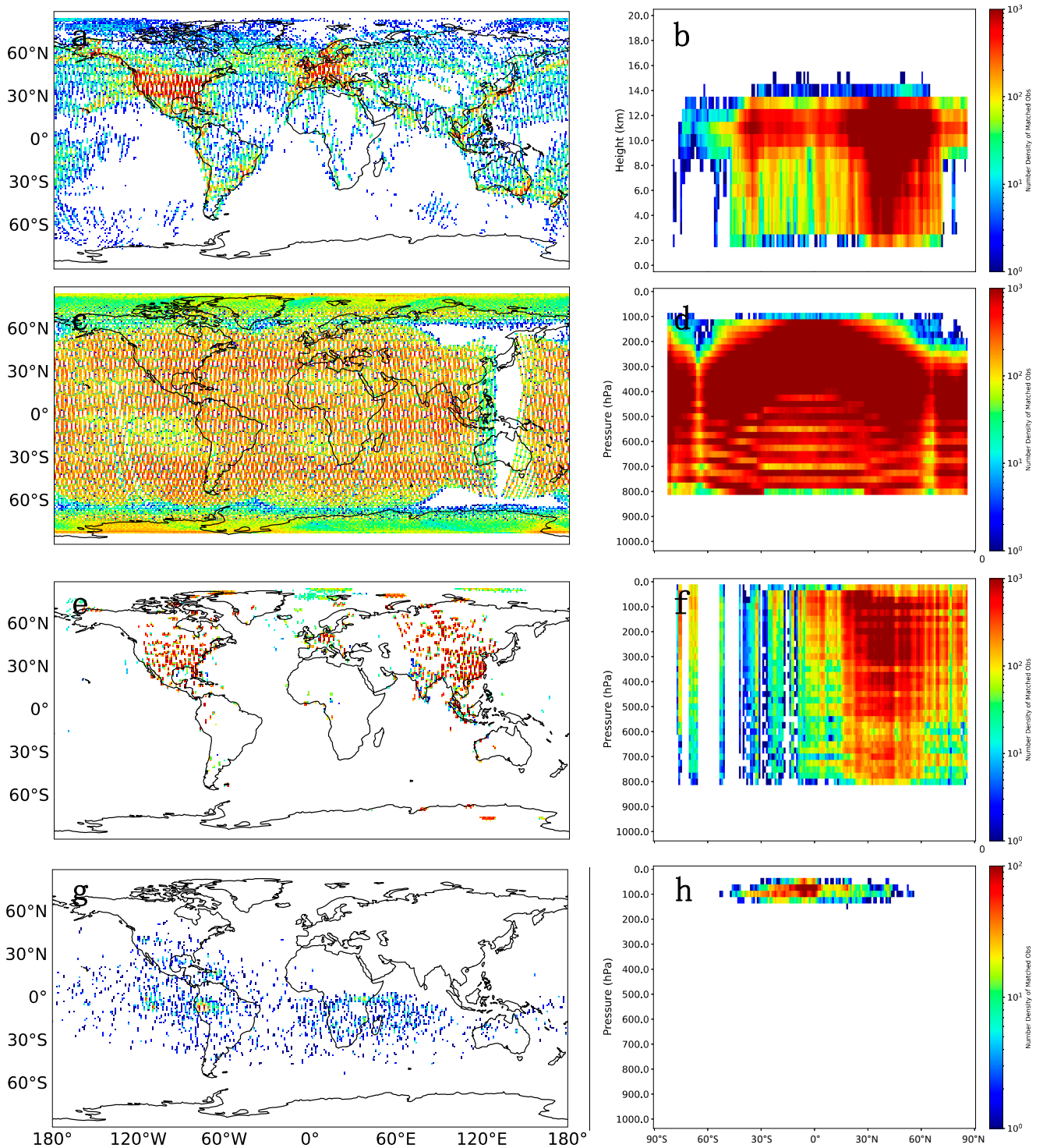


Figure 3. Observation number densities collapsed onto the latitude–longitude plane (left column) and onto the height/pressure–latitude plane (right column) for (a,b) aircraft winds, (c,d) AMVs, (e,f) sonde winds, and (g,h) Loon winds, all collocated with Aeolus Rayleigh-clear winds for September 2019–August 2020. The colors indicate the number density per grid cell, with dimensions of $1^\circ \times 1^\circ$ for panels (a,c,e,g), $1 \text{ km} \times 1^\circ$ for panel (b), and $25 \text{ hPa} \times 1^\circ$ for panels (d,f,h).

Figure 4 presents density scatterplot comparisons of global HLOS winds matched between the Driver (Aeolus RayClear on the left, MieCloud on the right) and one Dependent dataset (sondes) for the collocation period. The statistical results discussed here are summarized in Table 2 for all four Dependent datasets, and scatterplots for aircraft,

AMVs, and Loon are presented in the Supplementary Materials (Figure S3). In general, all four Dependent datasets match well with both Aeolus wind regimes, as illustrated by the observations falling near the one-to-one line that indicates a perfect match. The MieCloud comparisons have higher correlations and lower SD_Diffs than RayClear, consistent with the general higher accuracy of MieCloud winds, in agreement with the findings of several previous studies [46–48]. The density patterns for the MieCloud comparisons (e.g., Figure 4b) exhibit small asymmetries near the (0,0) point, due to calibration errors, which have recently been improved [38]. AMVs, aircraft, and sonde winds are all highly correlated (>0.9) with Aeolus, with aircraft exhibiting statistically significant differences from both Aeolus wind regimes, and AMVs being significantly different from RayClear winds. Loon winds exhibit the lowest correlation (0.84) and largest Mean_Diff ($|0.88|$ m/s) and SD_Diff (7.4 m/s) of the RayClear comparisons, as well as the smallest sample size (<8000 for Loon and >900,000 for the others). The magnitudes of the winds in the Loon collocation sample (Figure S3e) are smaller than those of the other independent wind datasets because (1) the Loon area, being in the Tropics, has generally lower wind speeds and (2) the super-obbing process averages over many Loon observations, resulting in lower wind speeds. Since the Loon winds are experimental, there may be opportunities to reduce their errors by reprocessing these data with enhanced methods to estimate the winds from the nearly error-free GPS location data.

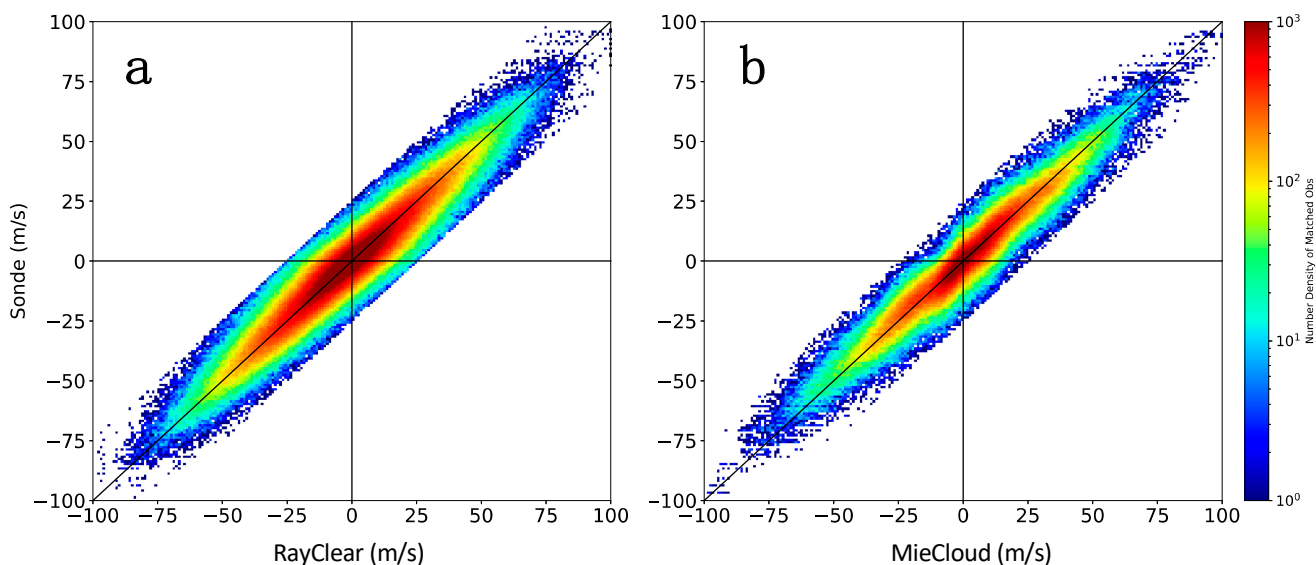


Figure 4. Density scatterplots of HLOS wind differences for RayClear (a) and MieCloud (b) comparisons with sondes for September 2019–August 2020. Statistics of the collocation are given in Table 2. The colors indicate the number density per $1 \text{ m/s} \times 1 \text{ m/s}$ cell.

Table 2. Statistics of the collocations presented in Figures 4 and 5. Sample statistics include collocation counts, correlation (r), and mean, standard deviation, and root mean square of HLOS wind difference (Mean_Diff, SD_Diff, and RMSD, respectively) in m/s. Mean_Diff in bold type are statistically significant at the 95% level.

Dependent	Driver	Count	r	Mean_Diff	SD_Diff	RMSD
Aircraft	RayClear	912,499	0.96	0.08	6.40	6.40
AMV	RayClear	5,317,244	0.93	0.14	7.25	7.25
Loon	RayClear	7413	0.84	−0.88	7.43	7.48
Sonde	RayClear	967,164	0.95	−0.06	6.49	6.49
Aircraft	MieCloud	568,322	0.98	0.21	5.56	5.56
AMV	MieCloud	8,601,138	0.97	−0.02	5.14	5.14
Sonde	MieCloud	490,391	0.96	−0.04	5.54	5.54

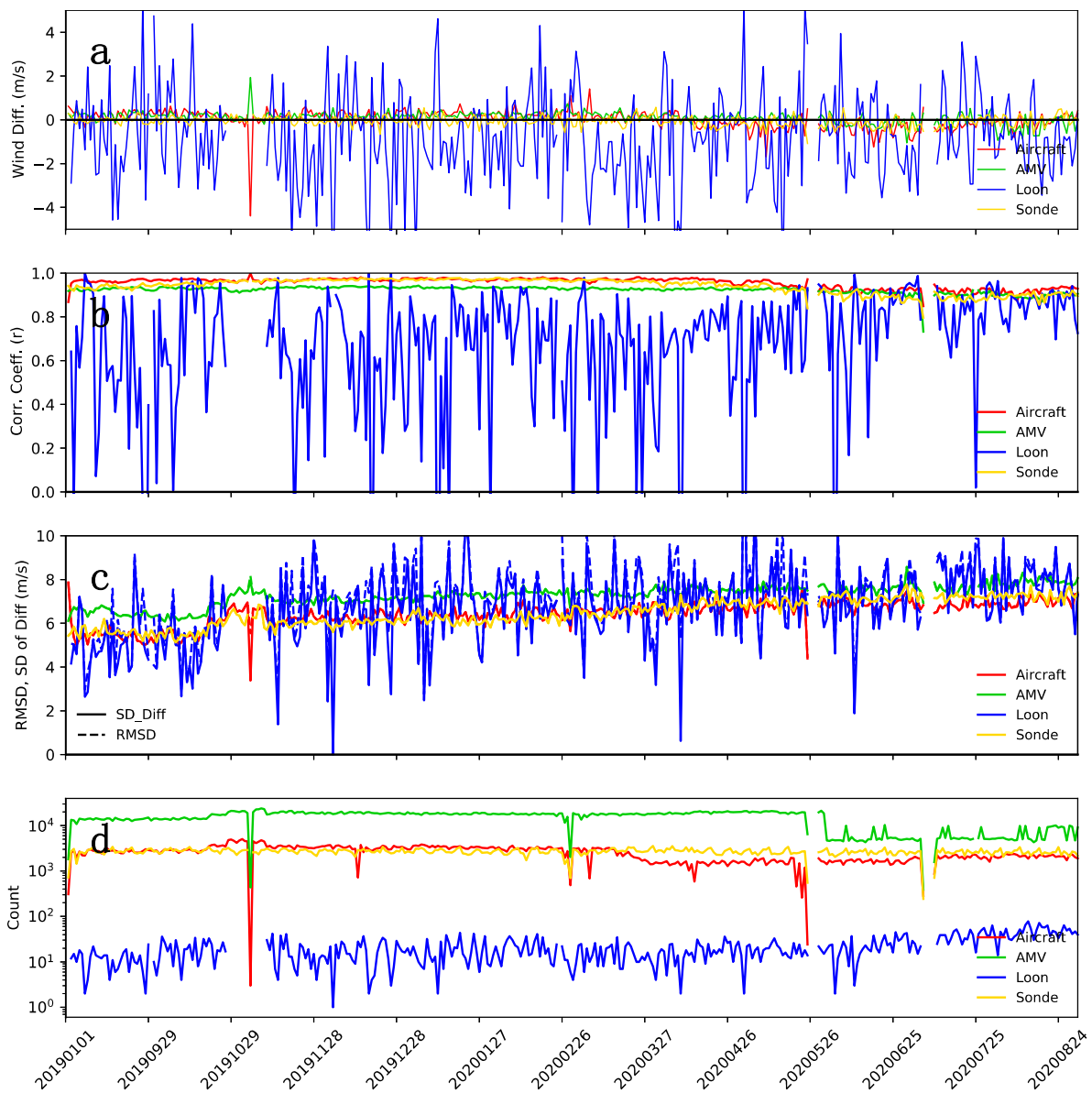


Figure 5. Time series of Mean_Diffs (m/s, (a)), correlation coefficients (r, (b)), RMSD and SD_Diffs (m/s, (c)), and collocation counts (d) for RayClear comparisons during September 2019–August 2020. Statistics of the collocation are given in Table 2. The colors denote each Dependent wind dataset.

Time series of global wind comparisons with RayClear are illustrated in Figure 5 (similar results for MieCloud are shown in the Supplementary Materials). RayClear Mean_Diffs are generally small throughout the study period (Figure 5a), and correlations are above 0.9 until June 2020, where they decrease slightly toward 0.8 (Figure 5b). This decrease corresponds to an increase in Mean_Diff magnitudes and SD_Diffs with time, as well as a decrease in the number of observations (Figure 5a,c,d), all of which are also observed when comparing the RayClear winds to the ECMWF model [46]. The increase in SD_Diffs can be explained by the observed signal loss along the instrument’s atmospheric path over time [46,48,49]. The Loon comparisons show the largest Mean_Diffs and SD_Diffs throughout the collocation period, as well as the lowest correlations and collocation counts. The MieCloud comparisons exhibit small Mean_Diffs, higher correlations, and smaller SD_Diffs (Figure S4) compared to RayClear, but there is no evident trend for MieCloud SD_Diffs. Note that the MieCloud Mean_Diffs increase with time (Figure S4a).

Mean vertical profiles of Mean_Diffs and SD_Diffs for the study period for the NH are shown in Figure 6 in the NH. The results for the Tropics and SH are shown in the Supplementary Materials (Figure S5). The RayClear Mean_Diffs are generally $< |1.0|$ m/s and are statistically significant throughout the vertical in each region (e.g., Figure 6a). The largest Mean_Diffs are observed in the mid- to lower troposphere (below 500 hPa), where the collocation counts are small. The RayClear Mean_Diffs trend from slightly positive near the surface to slightly negative aloft. The SD_Diffs are steady at 6–7 m/s throughout most of the atmospheric column and increase slightly above 200 hPa, which could be attributed to larger observation errors in the presence of high winds and stronger vertical wind shear, e.g., for AMVs [9]. The MieCloud comparisons (e.g., Figure 6c) show smaller Mean_Diffs ($< |0.5|$ m/s) and SD_Diffs (5–6 m/s) in the NH and TR. The notable exception is in the SH, where the Mean_Diffs are larger for all Dependent datasets ($\geq |1.0|$ m/s) and become larger with height. The MieCloud SD_Diffs increase with height and are likely attributed to larger observation errors at the upper levels due, in part, to a smaller sample size (e.g., Figure 6d) combined with high vertical wind shear (e.g., [50,51]).

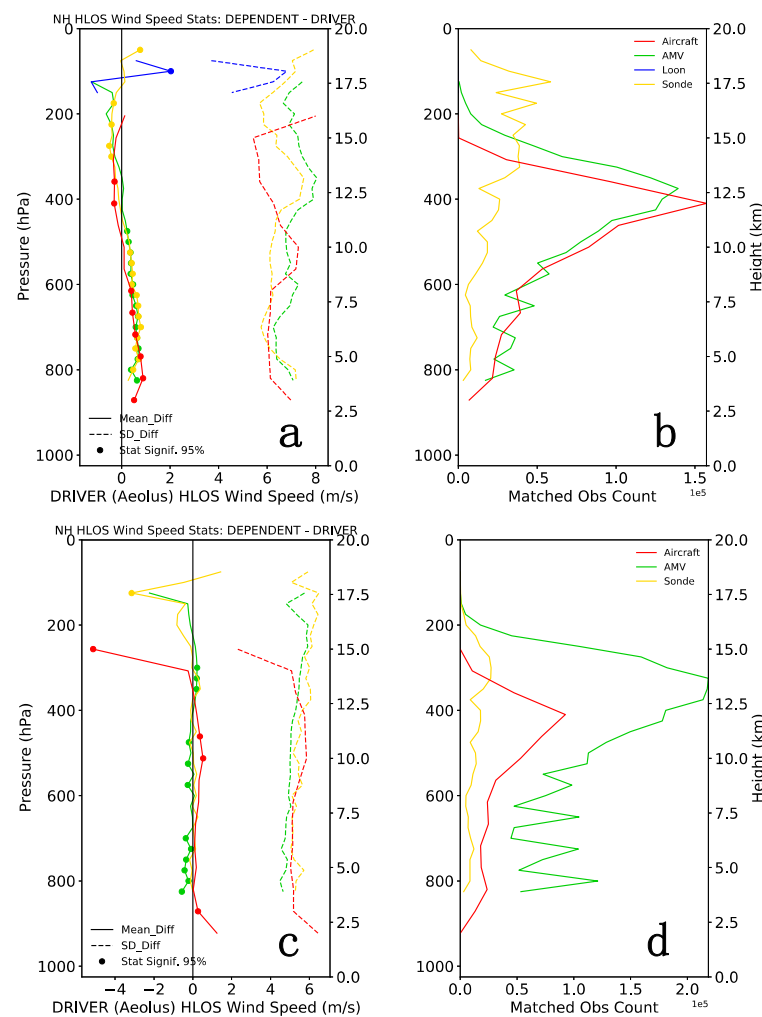


Figure 6. Vertical profiles of Mean_Diffs (solid lines) and SD_Diffs (dotted lines) per height/pressure level (left, (a,c)) and corresponding collocation counts ($1e5$, right, (b,d)) comparing the Dependent datasets (colors) with Aeolus RayClear (top, (a,b)) and MieCloud (bottom, (c,d)) winds for the NH during September 2019–August 2020. The solid dots indicate statistically significant Mean_Diffs at the 95% level.

Figure 7 displays the dependence of Mean_Diffs and SD_Diffs on Aeolus wind speed during the study period in the NH. The results for the Tropics and SH are shown in the Supplementary Materials (Figure S6). In general, the Mean_Diffs tend to become larger

for faster Aeolus winds for both Aeolus wind regimes. The RayClear comparisons (e.g., Figure 7a) have larger SD_Diffs that tend to increase with faster Aeolus winds relative to MieCloud (e.g., Figure 7c), again highlighting the general higher accuracy of MieCloud winds. This is particularly evident for AMVs (e.g., Figure 7a,c, green dashed lines) and in the SH, where there are fewer observations (Figure S6b,f). Furthermore, the SD_Diffs have similar values to the SDs of the Dependent datasets, implying that the Dependent wind quality governs the SD_Diffs. In addition, the collocation counts for all datasets (e.g., Figure 7b,d) peak to the right, where Aeolus HLOS velocities are positive, implying that many Dependent winds match Aeolus at upper levels, where westerly flow dominates. This is supported by the collocation counts displayed in Figure 6. The shift in peak counts exemplifies SAWC’s value in revealing the unique behavior of the data.

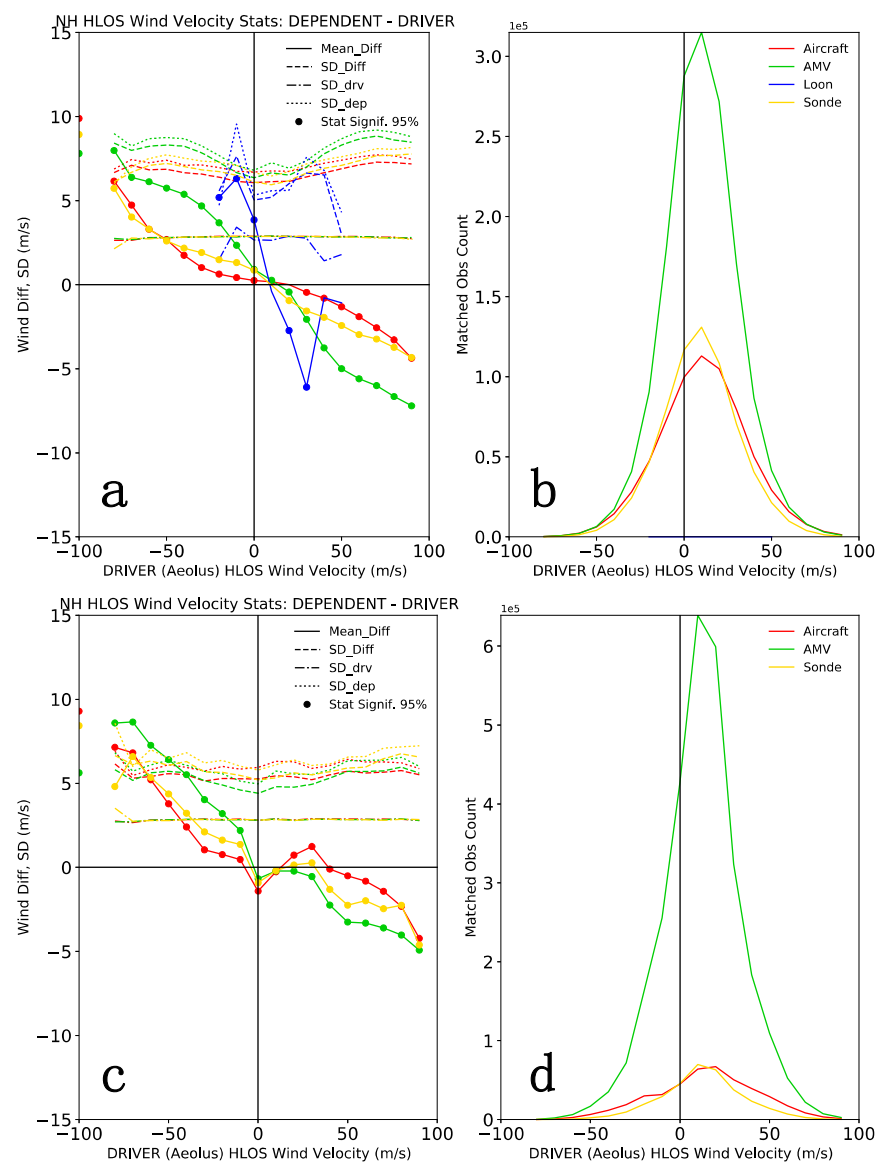


Figure 7. Mean_Diffs (solid lines), SD_Diffs (dotted lines), SDs of the Driver (dash-dot lines), and SDs of the Dependent datasets (dotted lines) (left, (a,c)) and corresponding collocations counts (1e5, right, (b,d)) as a function of the Driver wind speed (binned by 10 m/s) comparing the Dependent datasets (colors) with Aeolus RayClear (top, (a,b)) and MieCloud (bottom, (c,b)) winds for the NH during September 2019–August 2020. The solid dots indicate statistically significant Mean_Diffs at the 95% level.

3.1.2. AMV Wind Types vs. Aeolus

A unique capability of the SAWC plotting tool is the intercomparison of the following four main AMV wind types: IR, visible, WVclear, and WVcloud. AMV type comparisons are automatically performed only if the user selects an AMV dataset for analysis. Global and regional statistics are computed simultaneously. Figure 8 presents global density scatterplots of IR AMVs relative to Aeolus RayClear (left) and MieCloud winds (right) for the collocation period. The statistical results are summarized in Table 3 for all four types of AMVs, and scatterplots for the other three types of AMVs are presented in the Supplementary Materials (Figure S7). All AMV types match well with Aeolus, with each comparison exhibiting correlations of >0.9, and MieCloud comparisons exhibiting lower SD_Diffs (5–6 m/s) and higher correlations (>0.94) than RayClear, in agreement with our previous findings [25]. The Mean_Diffs are near zero, except for comparisons of winds from different scenes, e.g., the IR vs. RayClear comparison (Mean_Diff is 0.39 m/s) collocates cloud-tracked AMVs and Aeolus clear-scene winds, and the WVclear vs. MieCloud comparison (Mean_Diff is −0.66 m/s) collocates clear-sky AMVs and Aeolus cloudy-scene winds.

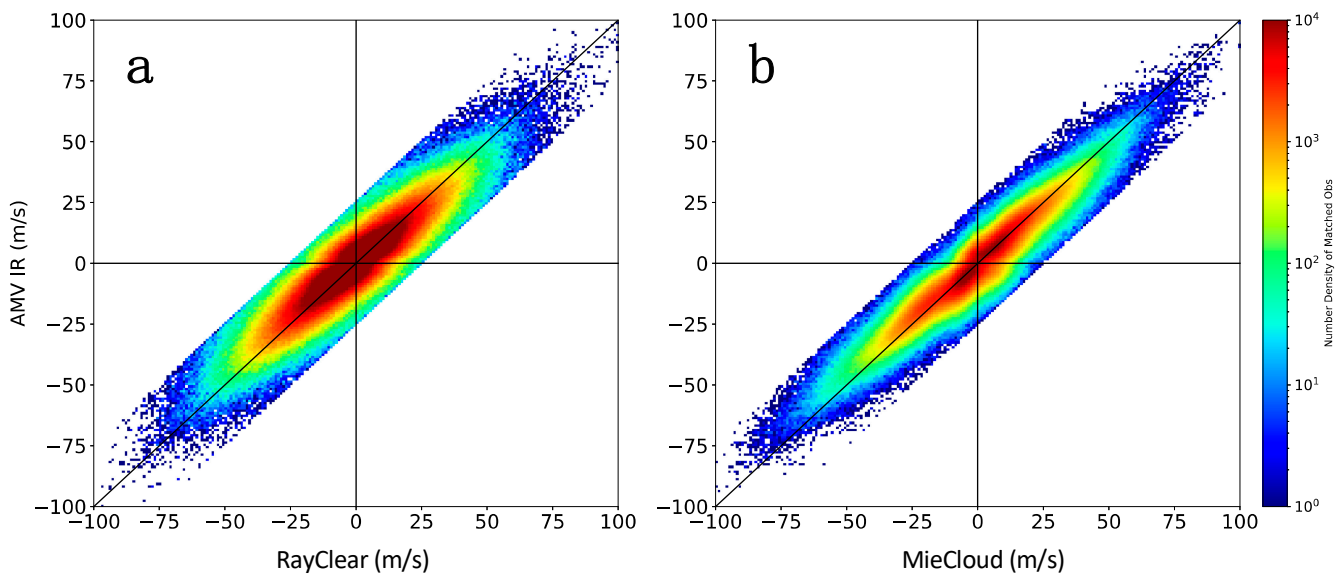


Figure 8. Density scatterplots of HLOS wind differences for RayClear (a) and MieCloud (b) as in Figure 4 but comparing Aeolus with IR AMVs. The statistics of the collocation are given in Table 3.

Table 3. Statistics of the collocations presented in Figure 8. As in Table 2 but for different AMV types.

Dependent	Driver	Count	r	Mean_Diff	SD_Diff	RMSD
IR	RayClear	1,532,395	0.90	0.39	7.03	7.04
Visible	RayClear	351,127	0.93	0.09	7.57	7.57
WVclear	RayClear	1,101,211	0.91	0.14	7.13	7.13
WVcloud	RayClear	848,455	0.93	0	7.81	7.81
IR	MieCloud	3,301,931	0.95	−0.14	5.06	5.06
Visible	MieCloud	675,493	0.97	0.01	5.27	5.27
WVclear	MieCloud	118,244	0.94	−0.66	5.83	5.87
WVcloud	MieCloud	851,981	0.97	−0.07	6.27	6.27

The mean vertical profiles of Mean_Diffs (AMV type minus Aeolus) and the corresponding SD_Diffs are shown per geographic region for the study period in Figures 9 and 10. The RayClear comparisons (Figure 9) exhibit similar Mean_Diff profiles in each region, as follows: larger, statistically significant differences (1–2 m/s) in the mid- to lower troposphere, where there are fewer collocations, and smaller statistically insignificant differences (<11 m/s) at pressure levels <400 hPa, where the collocation counts are higher. The SD_Diff profiles of IR and visible AMVs exhibit similar behavior, as follows: they are

steady at ~6 m/s in the lower troposphere, increase with height until 400 hPa, where they peak at 8 m/s, and decrease at upper levels. Likewise, WVcloud and WVclear SD_Diff profiles are similar in that they range from 8 to 10 m/s and tend to decrease with height throughout the troposphere.

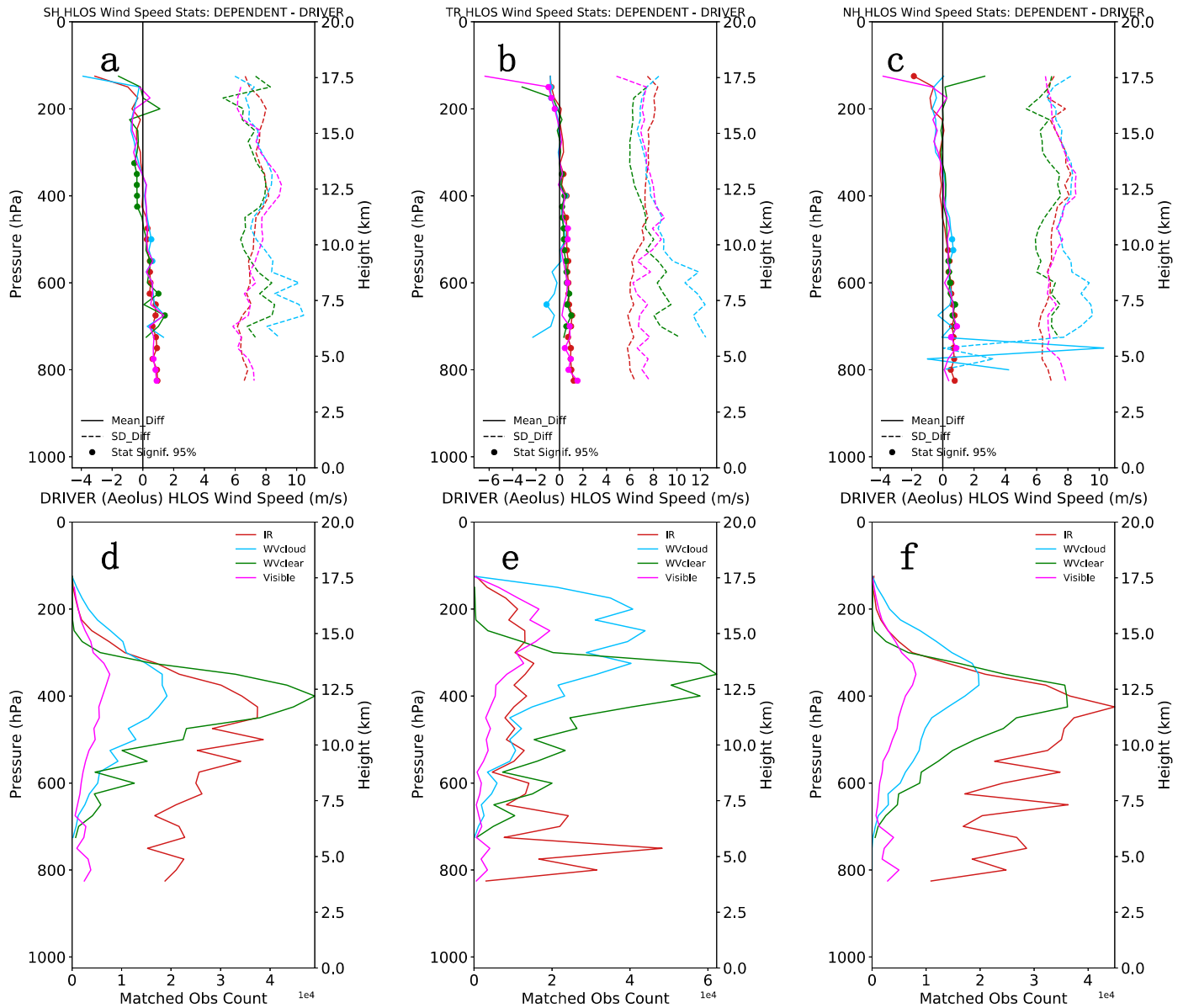


Figure 9. Vertical profiles of Mean_Diffs (solid lines) and SD_Diffs (dotted lines) per height/pressure level (top, (a–c)) and corresponding collocations counts (1e4, bottom, (d–f)) comparing the Dependent datasets (colors) with Aeolus RayClear winds for the SH (left, (a,d)), Tropics (center, (b,e)), and NH (right, (c,f)) during September 2019–August 2020. The solid dots indicate statistically significant Mean_Diffs at the 95% level. Plotting conventions are the same as those in Figure 6.

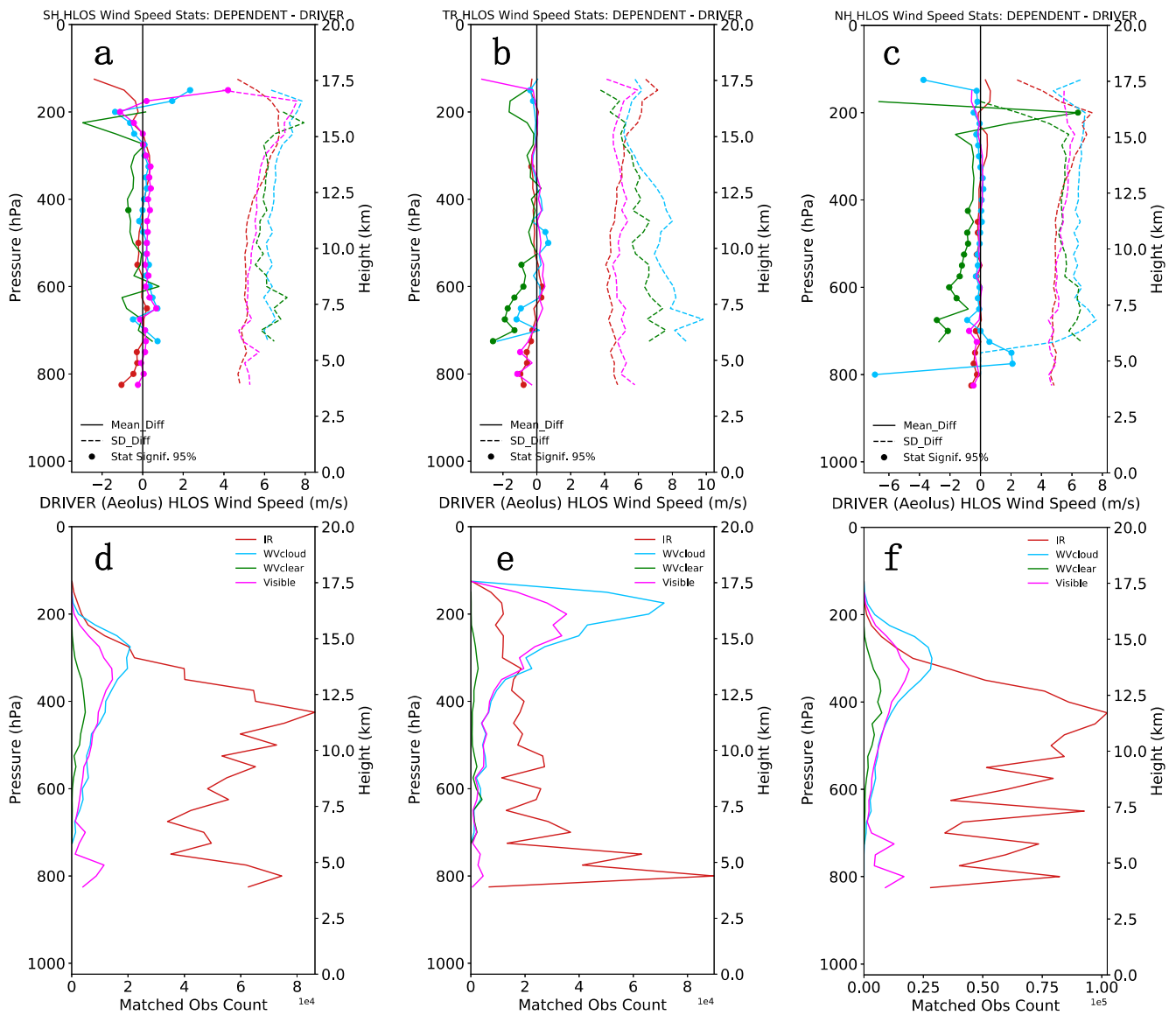


Figure 10. Vertical profiles of statistics comparing IR, visible, WVcloud, and WVclear AMVs with Aeolus MieCloud winds. Otherwise as in Figure 9.

Unlike RayClear, the MieCloud profiles (Figure 10) exhibit different behaviors in each geographic region. The Mean_Diffs in the NH (Figure 10c) and TR (Figure 10b) are larger (−1 to −2 m/s) and statistically significant in the mid- to lower troposphere, where there are fewer collocations. In the upper troposphere (pressures < 400 hPa), the Mean_Diffs are near zero and not statistically significant, except for WVcloud in the NH. The MieCloud SD_Diff profiles exhibit similar behavior to their RayClear counterparts, as follows: the IR and visible SD_Diffs are relatively constant throughout most of the atmospheric column, while the WVcloud and WVclear profiles exhibit larger values at lower levels and decrease at a faster rate with height. This is particularly evident in the TR (Figure 10a). In the SH (Figure 10b), the MieCloud Mean_Diffs are relatively small (around 1 m/s) and statistically significant throughout the vertical. The SD_Diffs range from 5 to 7 m/s at lower levels and increase with height for all AMV types, particularly at pressures of < 400 hPa. This behavior is consistent with the results discussed in [25] and could be attributed to height assignment errors at near-jet levels, as AMV uncertainties tend to increase in areas with higher wind speed and stronger shear [50–52].

3.1.3. Aircraft vs. Aeolus during the COVID-19 Pandemic

SAWC is capable of providing insight into the environmental impact of unprecedented global events, such as the COVID-19 pandemic. The COVID-19 pandemic effectively shut down the globe, beginning in March 2020. Several facets of the global economy were heavily impacted, particularly air travel, which was considerably reduced. Studies have since examined the pandemic's effect on aircraft observations during this time and the subsequent impact of the reduction in aircraft data on the climate, atmospheric composition, and NWP [45,53–57].

Figure 11 presents an examination of the pandemic's impact on aircraft data quality. SD_Diffs of aircraft versus Aeolus RayClear winds on a height–latitude plane are shown in the left column of Figure 11 for four 3-month periods, and the corresponding number densities or counts per grid cell are displayed in the right column. Before the pandemic (SON and DJF, Figure 11a,c), the SD_Diffs were generally 5–8 m/s in the mid- to upper troposphere (6–12 km) and throughout the NH, where the majority of winds are collocated. During the pandemic (MAM and JJA, Figure 11e,g), the SD_Diffs increased at upper levels (8–12 km), where the number of collocations decreased, particularly in the NH in JJA (Figure 11h). Prior to the onset of the pandemic (SON and DJF, Figure 11b,d), the number of collocations per season remained relatively constant, at around 290,000, with many observed in the NH and upper troposphere, as expected. After the pandemic began (MAM and JJA, Figure 11f,h), the total number of collocations decreased by over 50%, reflecting the substantial aircraft data gap that emerged as a result of the pandemic's impact on air travel [45,56]. This is particularly evident during JJA in the TR and SH, where the number of aircraft wind profiles is largely reduced. The MieCloud comparisons exhibit similar patterns (not shown). These results are consistent with the findings that the reduction in the number of commercial aircraft flights and, therefore, the number of high-quality aircraft wind observations during the pandemic, had a considerable negative impact on regional NWP forecast skill [45,56,58,59].

3.2. Observation Error Estimation for Data Assimilation

SAWC's utility extends beyond wind comparison statistics, e.g., observation error estimation that is critical for data assimilation (DA). For example, SAWC can be used to investigate how well DA observation errors match actual observation collocation difference standard deviations. An example of this is presented in Figure 12, which shows global mean observation error estimates per Aeolus MieCloud wind speed bin during the collocation period. The variance for Aeolus (dash-dot lines) is computed using observation error values provided by ESA. The variance for each Dependent dataset (dotted lines) is computed using input observation errors in NOAA operations. The total variance (solid lines) equals the Aeolus variance plus the Dependent variance. The square of the mean wind difference (Dependent minus Driver) that is computed in SAWC is displayed as dashed lines. Ideally, the total variance and the square of the difference should be nearly identical, implying that the observation error covariance estimates in DA match the observations. For aircraft and sondes, this is the case for slower winds ($<|25|$ m/s) when using a single observation error value (3.0 m/s) for all winds in each dataset. However, wind errors increase with wind speed, and this is particularly apparent here where the results are presented by wind speed bins.

AMV error covariance estimation is challenging. It is clear in Figure 12a that the use of a single observation error value (10 m/s) is not ideal, as the total variance and square of the difference differ by ~10–100 m/s. When using a range of vertically varying errors (Figure 12b), the results improve, as the shape of the total AMV variance is similar to that of the square of the mean wind difference; however, their magnitudes still greatly differ for most observations. Further investigation into AMV error covariance characterization is out of the scope of this work; however, it is necessary and strongly recommended for future studies.

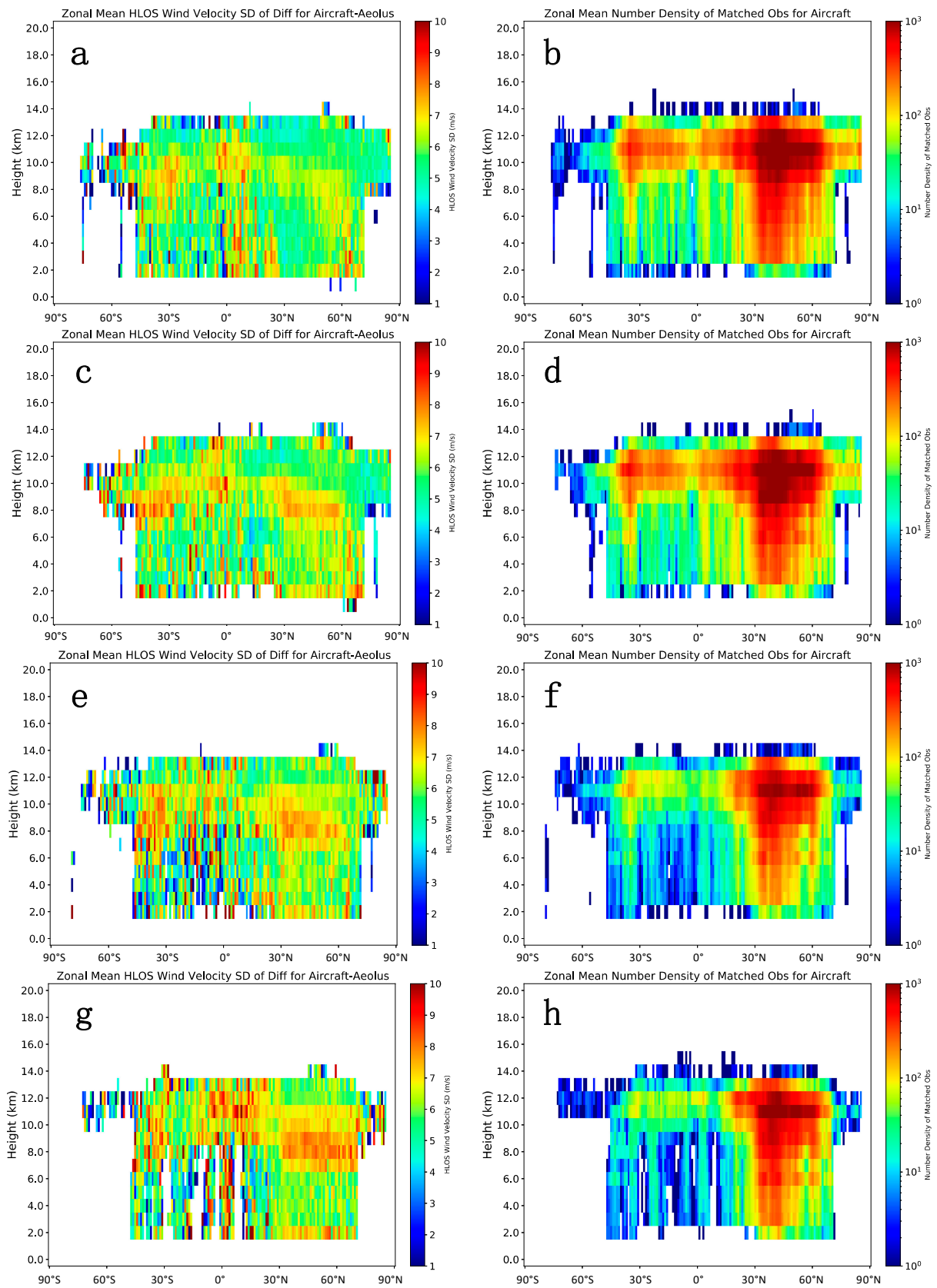


Figure 11. Height–latitude plots of aircraft vs. Aeolus RayClear SD_Diffs in m/s (left (a,c,e,g)) and corresponding collocation counts (right (b,d,f,h)) during September 2019–August 2020, stratified by 3-month seasons: (a,b) SON, (c,d) DJF, (e,f) MAM, and (g,h) JJA. Each grid cell is $1 \text{ km} \times 1^\circ$.

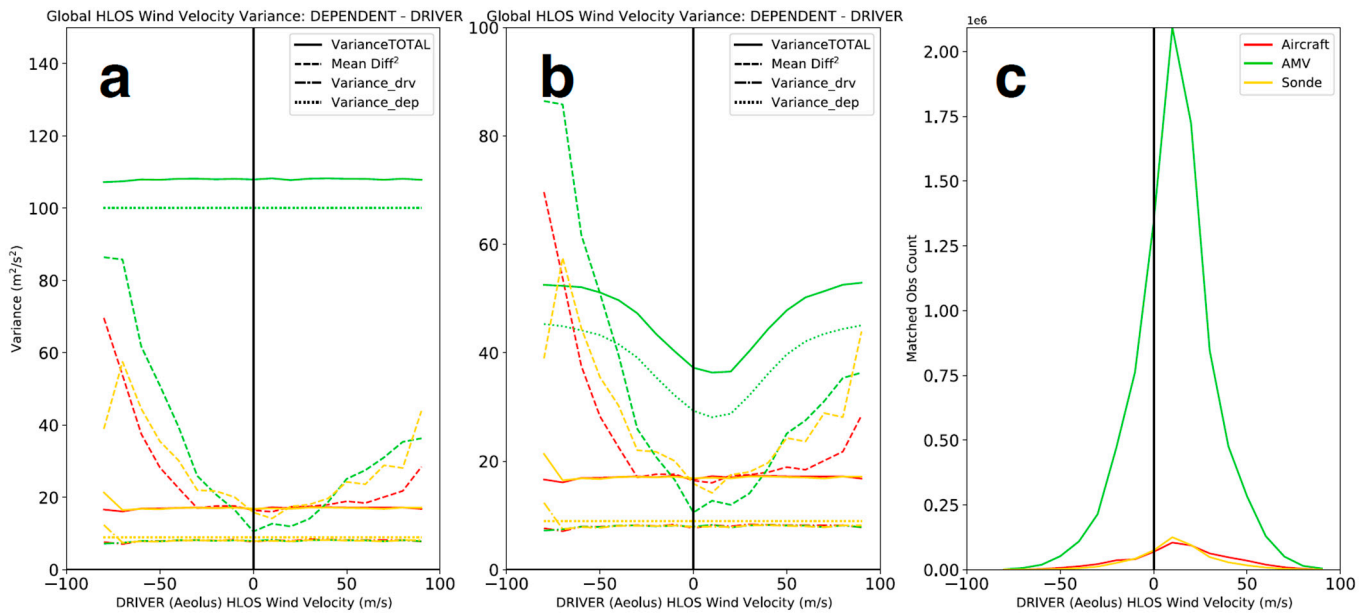


Figure 12. Global mean observation error variance estimates (a,b) and corresponding collocation counts (1e6, (c)) vs. Driver wind speed binned by 10 m/s comparing the Dependent datasets (colors) with Aeolus MieCloud winds during September 2019–August 2020. For variance estimates: Error variance of the Driver (dash-dot lines) using observation error values from the data producers, error variance of the Dependent datasets (dotted lines) using observation errors that are used as input in NOAA operations, total variance that equals the Driver variance plus the Dependent variance (solid lines), and the square of the mean wind difference (Dependent–Driver) computed in SAWC (dashed lines). In (a), Dependent observation errors in each dataset are set to a single value for all winds: Aircraft = 3.0 m/s, Sonde = 3.0 m/s, AMV = 10 m/s. In (b), aircraft and sonde errors are the same as in (a), but the AMV observation error is set to a range of vertically varying values from 3.8 m/s at pressures >1000 hPa to 7.0 m/s at pressures <250 hPa, and represents the median range of input observation errors used for each satellite in NOAA operations.

4. Summary and Discussion

This article introduces the System for Analysis of Wind Collocations (SAWC) that was jointly developed by NOAA/NESDIS/STAR, UMD/CISESS, and UW-Madison/CIMSS to support users’ needs to acquire and analyze wind data from multiple sources and to further address the requirement for highly accurate 3D winds put forth in the National Academies’ 2017–2027 decadal survey [1]. SAWC’s end-to-end process can be described in the following three steps (Figure 1):

1. Data Acquisition, where wind observations are acquired from aircraft, satellites (Aeolus winds and AMVs), sondes, and stratospheric superpressure balloons (Figure S1); converted to a common format (netCDF); and archived.
2. Collocation of Winds, where users can utilize the SAWC collocation tool developed for their intercomparison to produce a collection of matched winds between different datasets.
3. Analysis and Visualization, where users can interact with the SAWC plotting tool to visually and statistically compare the matched winds based on their research needs.

To demonstrate the utility of SAWC, a one-year evaluation compared Aeolus winds to other wind datasets. As discussed earlier (start of Section 3.1), Aeolus provides winds with uniform global coverage, which helps to fill in the gaps in wind profiles over the ocean and the Southern Hemisphere. Aeolus (i.e., the Driver dataset) was compared to the following four other wind datasets available in the SAWC archive at the time of writing: AMV, aircraft, sonde, and Loon stratospheric balloon winds (Dependent datasets). The wind vectors from the non-Aeolus datasets are projected onto the Aeolus HLOS for the comparisons. SAWC can also compare full vector winds, for example, aircraft vs. AMVs, or sondes vs. aircraft.

The results show that the matched winds have regional to near-global spatial coverage that varies for each Dependent dataset (Figure 3 and S2). The statistical comparisons highlight that the Dependent datasets match well with both Aeolus Rayleigh-clear and Mie-cloudy wind regimes for the study period (Figure 4 and S3), with Mie-cloudy comparisons exhibiting smaller standard deviations of wind differences (SD_Diffs) relative to Rayleigh-clear, which is consistent with the higher accuracy of Mie-cloudy winds [46]. The SD_Diffs for Rayleigh-clear comparisons increase over time due to the degradation in the Aeolus retrieval signals [46,48,49] (Figure 5 and S4). The mean wind differences (Mean_Diffs) in the NH and TR are relatively small throughout the vertical for both Aeolus wind regimes (< 1.0 m/s), and SD_Diffs remain relatively constant (5–7 m/s) (Figure 6 and S5). SH Mean_Diffs are larger and corresponding SD_Diffs generally increase with height, as well as for faster winds (Figure 7 and S6).

In addition, SAWC was used to compare individual AMV wind types to Aeolus (Figures 8–10 and S7). Mie-cloudy comparisons with IR, visible, WV clear sky, and WV cloudy sky AMVs each show lower SD_Diffs (5–6 m/s) and higher correlations (> 0.94) than Rayleigh-clear, in agreement with our previous findings [25]. In the vertical, SD_Diffs for IR and visible AMVs remain relatively constant, while the WV cloudy sky and WV clear sky profiles show larger values that tend to decrease with height, except in the SH, where all SD_Diff profiles generally increase with height.

The collocation period chosen afforded the unique opportunity to showcase SAWC's capability in providing insight into aircraft wind observation data quality after the onset of the COVID-19 pandemic. A seasonal analysis highlights the reduced coverage of aircraft observations after the pandemic began in March 2020. The SD_Diffs between aircraft and Aeolus winds increased at upper levels, where the observation counts were noticeably reduced (Figure 11), implying a degradation in data quality. The results are consistent with recent findings [45,56], in that the dearth of available aircraft observations during the pandemic contributed to poorer data quality. In addition, to demonstrate SAWC's utility beyond intercomparisons, a brief example of how SAWC could be used to support observation error estimation in DA systems was presented (Figure 12).

The potential value of SAWC is wide-ranging, from product validation and observation error characterization to advancements in the global Earth observing architecture. Moreover, SAWC could also be employed to test and establish new wind collocation standards, as has been recommended in order to keep up with advances in wind retrieval technologies and numerical weather prediction systems (e.g., AMV algorithm improvements, higher-resolution observations, and advanced global DA systems). The collocation and plotting tools are flexible and designed to handle additional wind datasets that are not yet available in the archive, e.g., radial winds. Since radial winds are similar in form to Aeolus winds, in that the winds are retrieved along one direction, the Aeolus HLOS projection algorithm could also be applied to radial winds (see Appendix B). At present, the SAWC collocation and plotting tools can only handle point observation wind datasets. Gridded datasets (e.g., NWP reanalyses) could be added to SAWC. Gridded datasets allow interpolation to the observation location and time, thereby eliminating collocation errors; however, gridded data are often large scale compared to observations, thereby increasing representativeness errors. Future iterations of SAWC may include other observational products such as cloud optical and physical parameters that are important to AMVs and DWLs. SAWC is publicly available and is hosted online by NOAA/NESDIS/STAR at <https://www.star.nesdis.noaa.gov/sawc> (accessed on 28 February 2024).

Supplementary Materials: The following supporting information can be downloaded at: <https://www.mdpi.com/article/10.3390/meteorology3010006/s1>, Figure S1: Example spatial coverage of each wind dataset currently available in the SAWC archive; Figure S2: Observation number densities of aircraft, AMVs, and sonde winds all collocated with Aeolus Mie-cloudy winds; Figure S3: Density scatterplots of HLOS wind differences for Aeolus compared with aircraft, AMVs, and sonde winds; Figure S4: Time series of wind difference statistics for Aeolus Mie-cloudy comparisons; Figure S5: Vertical profiles of wind difference statistics comparing the Dependent datasets with Aeolus in the SH and Tropics; Figure S6: Wind difference statistics as a function of Aeolus wind speed in the SH and Tropics; Figure S7: Density scatterplots of HLOS wind differences for Aeolus compared with visible, WV clear-sky, and WV cloudy-sky AMVs.

Author Contributions: K.G. and K.I. proposed the project as co-investigators and provided the expertise that guided this work. B.H. and D.S. developed the collocation algorithm used. B.H. built the foundation for the SAWC collocation software application. K.E.L. performed most of the work that included comparison analyses and major updates to the application's collocation and plotting tools. D.H. contributed a substantial upgrade to the collocation tool that greatly improved its cost efficiency. D.S., R.N.H., and H.L. provided additional intellectual support that considerably improved the article. K.E.L. prepared the paper, with contributions from all coauthors. All authors have read and agreed to the published version of the manuscript.

Funding: This research was supported by the NOAA/NESDIS Office of Projects, Planning, and Acquisition (OPPA) Technology Maturation Program (TMP) through the Cooperative Institute for Climate and Satellites (CICS) and the Cooperative Institute for Satellite Earth System Studies (CISESS) at the University of Maryland (UMD)/Earth System Science Interdisciplinary Center (ESSIC) (grant nos. NA14NES4320003 and NA19NES4320002) and the Cooperative Institute for Meteorological Satellite Studies (CIMSS) at the University of Wisconsin-Madison (UW-Madison) (grant no. NA20NES4320003).

Data Availability Statement: All data used in this work are publicly available at <https://www.star.nesdis.noaa.gov/data/sawc> (accessed on 28 February 2024).

Acknowledgments: The authors thank ESA, ECMWF, the NCEP/EMC ObsProc team, and Max Kamenetsky, James Antifaev, Sal Candido, Rob Carver and the rest of the team at Loon, LLC, for providing the data; Peter Marinescu for his contributions towards converting Aeolus BUFR data into 6-h NCEP prepBUFR for the purpose of data assimilation in NOAA NWP; Szuchia Moeller for her contribution towards the initial development of tools for analysis and visualization; Iliana Genkova, Jim Jung, Jaime Daniels, Cathy Thomas, and Emily Liu for their expertise on NCEP prepBUFR and winds in NOAA NWP; the Aeolus Cal/Val teams, Mike Hardesty, Erin Jones, Chris Barnett, and Sebastian Bley for their scientific and technical expertise; and Sid Boukabara for his leadership and support of this project. The authors thank the administrators of the S4 supercomputer [60] at UW-Madison's Space Science Engineering Center (SSEC) who provided the groundwork for SAWC's initial development. The authors also thank Lori Brown, Brian Keffer, Donovan Kelly, and the rest of the information technology (IT) administrators at the NOAA/NESDIS/Center for Satellite Applications and Research (STAR) for their continued support in hosting and maintaining SAWC at STAR. The scientific results and conclusions, as well as any views or opinions expressed herein, are those of the authors and do not necessarily reflect those of NOAA or the U.S. Department of Commerce.

Conflicts of Interest: Brett Hoover was employed by Lynker Technologies, David Huber was employed by Redline Performance Solutions. The remaining authors declare that the research was conducted in the absence of any commercial or financial relationships that could be construed as a potential conflict of interest. The funders had no role in the design of the study; in the collection, analyses, or interpretation of data; in the writing of the manuscript; or in the decision to publish the results.

Appendix A

Characteristics of the SAWC collocation application are summarized in the following tables.

Table A1. List of SAWC management components: index files and the collocation software application. N/A indicates not applicable.

SAWC Component	Formats	Temporal Coverage	Key Variables Available
Index Files	NetCDF-4 files	Select periods	Indices of matched winds; Differences in time, height/pressure, and distance for each pair of matched winds
Collocation Application	One tarball per application version, each containing Bash and Python scripts	N/A	N/A

Table A2. List of main input parameters that the user can modify in the collocation tool.

Collocation Tool Parameter	Description
Date Range	Year, month, and range of days over which to run the collocation tool.
Dataset Names	Names of datasets to be collocated. (The first dataset listed is the Driver; all others are Dependents)
Path to Output Index Files	Full path to location where output collocation index files are to be saved.
Collocation Criteria	Four criteria: Max collocation distance in km; Max time difference in minutes; Max log ₁₀ (pressure) difference log ₁₀ (hPa); Max height difference in km. (Must have four criteria per Dependent dataset to be collocated)
Quality Control Flags	Quality control (QC) flags for each dataset (Driver and Dependents) indicating whether or not QC will be applied. Options: 0 (no QC applied); 1 (QC applied)
Number of Matches Allowed	Number of Dependent observations allowed to match each Driver observation. Default = 50
AMV Quality Indicator	Quality indicator (QI) value in % for AMV observations.
AMV Quality Indicator Option	QI options for AMVs: Use QI variable without the forecast (NO_FC default); Use QI variable with the forecast (YES_FC)
Aeolus Dataset Type	Abbreviation for Aeolus L2B dataset type. Options: orig (dataset processed with original L2B processor at time of retrieval); B## (dataset reprocessed with a different L2B processor than that used at time of retrieval, where ## is a 2-digit number indicating the Baseline number, e.g., B10 = Baseline 10)

Table A3. Wind-community-recommended QC parameters currently available in SAWC that are applied to the listed datasets only if the user selects this option. Default reject values are listed in the table. For Aeolus, *p* is pressure in hPa, *sigma* is the L2B uncertainty in m/s, *z* is the height of the vertical range bins within which measurements are accumulated, and length is the integration length in km over which the measurements are accumulated. For AMVs, the quality indicator (QI) is the minimal acceptable percent confidence value (in %).

Dataset	QC Parameters
Aeolus Mie-cloudy	$p > 800$ hPa; $\sigma > 5$ m/s
Aeolus Rayleigh-clear	$p > 800$ hPa; $\sigma > 8.5$ m/s for $800 \geq p > 200$ hPa; $\sigma > 12$ m/s for $p \leq 200$ hPa; $z < 0.3$ km; length < 60 km
AMV	QI < 80

Table A4. Default collocation criteria applied to each listed dataset. t in minutes indicates the maximum time difference allowed between the Driver and Dependent observations; x in km is the maximum great circle distance allowed from the Driver observation; p and z are the maximum pressure difference (in hPa) and height difference (in km), respectively, allowed between the Driver and Dependent observations. Note that the collocation tool opts to compute pressure differences over height differences: height differences are calculated only if the pressure variable is not available in either or both the Driver and Dependent datasets.

Dataset	Δt	Δx	Δp	Δz
Aeolus	60 min	100 km	0.04 log10 (hPa)	1 km
Aircraft	60 min	100 km	0.04 log10 (hPa)	1 km
AMV	60 min	100 km	0.04 log10 (hPa)	1 km
Loon	60 min	100 km	0.04 log10 (hPa)	1 km
Sonde	90 min	150 km	0.04 log10 (hPa)	1 km

Table A5. List of main input parameters the user can modify in the plotting tool.

Parameter	Description
Start Date, End Date	Start date and end date (year, month, day, hour) over which to run the collocation tool.
Driver Dataset Name	Name of Driver dataset.
Dependent Dataset Names	Names of Dependent datasets to be compared to the Driver.
Path to Input Index Files	Full path to location where input collocation index files are located.
Path to Output Plots	Full path to location where output plots are to be saved.
Super-ob Choice	Choice to super-ob (average) multiple collocations per Driver observation or use all collocations for statistical analysis. Options: -1 (use all collocations) or 0 (super-ob).

Appendix B

If Aeolus is included in the wind comparison as either the Driver or a Dependent dataset, the non-Aeolus winds that are matched with Aeolus are projected onto the Aeolus HLOS wind direction prior to any statistical analysis or plotting taking place. If Aeolus is the Driver, all Dependent winds are projected onto the HLOS direction, and all statistical analyses are computed using the HLOS-projected winds. If Aeolus is listed as a Dependent dataset, the matched Driver winds are projected onto the HLOS direction, and statistical analyses only concerning Aeolus are computed using the HLOS-projected winds; otherwise, the Driver–Dependent matches are compared using the wind data as is.

The projection of non-Aeolus winds y onto the Aeolus HLOS direction x_{dir}^{HLOS} is provided in Equations (A1)–(A4), as follows:

$$u_y = -y_{spd} \sin(y_{dir}) \tag{A1}$$

$$v_y = -y_{spd} \cos(y_{dir}) \tag{A2}$$

$$y_{spd}^{HLOS} = (-u_y \sin(x_{dir}^{HLOS})) + (-v_y \cos(x_{dir}^{HLOS})) \tag{A3}$$

$$y_{dir}^{HLOS} = x_{dir}^{HLOS} \tag{A4}$$

where y_{spd} and y_{dir} are the non-Aeolus wind speed and direction, respectively, u_y and v_y are the u - and v -components of the non-Aeolus wind, respectively, y_{spd}^{HLOS} is the non-Aeolus wind vector projected onto the HLOS direction, and y_{dir}^{HLOS} is the new direction of the non-Aeolus wind and is equal to the HLOS direction x_{dir}^{HLOS} .

References

1. National Academies of Sciences, Engineering, and Medicine. *Thriving on Our Changing Planet: A Decadal Strategy for Earth Observation from Space*; National Academies Press: Washington, DC, USA, 2018. [CrossRef]
2. Hertzog, A.; Basdevant, C.; Vial, F. An assessment of ECMWF and NCEP-NCAR Reanalyses in the Southern Hemisphere at the end of the presatellite era: Results from the EOLE experiment (1971–1972). *Mon. Weather. Rev.* **2006**, *134*, 3367–3383. [CrossRef]
3. Morel, P.; Bandeen, W. The Eole experiment: Early results and current objectives. *BAMS* **1973**, *54*, 298–306. [CrossRef]
4. Rabier, F.; Bouchard, A.; Brun, E.; Doerenbecher, A.; Guedj, S.; Guidard, V.; Karbou, F.; Peuch, V.H.; Amraoui, L.E.; Puech, D.; et al. The CONCORDIASI project in Antarctica. *Bull. Am. Meteorol. Soc.* **2010**, *91*, 69–86. [CrossRef]
5. Rhodes, B.; Candido, S. Loon Stratospheric Sensor Data [Dataset]. Zenodo. 2021. Available online: <https://zenodo.org/records/5119968> (accessed on 19 October 2023).
6. Velden, C.S.; Hayden, C.M.; Nieman, S.J.; Menzel, W.P.; Wanzong, S.; Goerss, J.S. Upper-tropospheric winds derived from geostationary satellite water vapor observations. *BAMS* **1997**, *78*, 173–195. [CrossRef]
7. Santek, D.; García-Pereda, J.; Velden, C.; Genkova, I.; Wanzong, S.; Stettner, D.; Mindock, M. A new atmospheric motion vector intercomparison study. Technical Report. In Proceedings of the 12th International Winds Workshop, Copenhagen, Denmark, 16–20 June 2014; Available online: <http://www.nwcsaf.org/aemetRest/downloadAttachment/225> (accessed on 18 December 2020).
8. Santek, D.; Dworak, R.; Nebuda, S.; Wanzong, S.; Borde, R.; Genkova, I.; García-Pereda, J.; Negri, R.G.; Carranza, M.; Nonaka, K.; et al. 2018 Atmospheric Motion Vector (AMV) Intercomparison Study. *Remote Sens.* **2019**, *11*, 2240. [CrossRef]
9. Cotton, J.; Doherty, A.; Lean, K.; Forsythe, M.; Cress, A. NWP SAF AMV Monitoring: The 9th Analysis Report (AR9). Technical Report, NWP SAF 2020, Version 1.0, REF: NWPSAFMO-TR-039. Available online: <https://nwp-saf.eumetsat.int/site/monitoring/winds-quality-evaluation/amv/amv-analysis-reports/> (accessed on 9 May 2021).
10. Reitebuch, O.; Lemmerz, C.; Nagel, E.; Paffrath, U.; Durand, Y.; Endemann, M.; Fabre, F.; Chaloupy, M. The Airborne Demonstrator for the Direct-Detection Doppler Wind Lidar ALADIN on ADM-Aeolus. Part I: Instrument Design and Comparison to Satellite Instrument. *J. Atmos. Ocean. Technol.* **2009**, *26*, 2501–2515. [CrossRef]
11. Stoffelen, A.; Pailleux, J.; Källén, E.; Vaughan, J.M.; Isaksen, L.; Flamant, P.; Wergen, W.; Andersson, E.; Schyberg, H.; Culoma, A.; et al. The atmospheric dynamics mission for global wind field measurement. *BAMS* **2005**, *86*, 73–87. [CrossRef]
12. Velden, C.S.; Holmlund, K. Report from the working group on verification and quality indices (WG II). In Proceedings of the 4th International Winds Workshop, Saanenmöser, Switzerland, 20–23 October 1998. Available online: https://cimss.ssec.wisc.edu/iwgg/iww4/p19-20_WGReport3.pdf (accessed on 5 January 2022).
13. Bedka, K.M.; Velden, C.S.; Petersen, R.A.; Feltz, W.F.; Mecikalski, J.R. Comparisons of Satellite-Derived Atmospheric Motion Vectors, Rawinsondes, and NOAA Wind Profiler Observations. *J. Appl. Meteorol. Clim.* **2009**, *48*, 1542–1561. [CrossRef]
14. Velden, C.S.; Bedka, K.M. Identifying the Uncertainty in Determining Satellite-Derived Atmospheric Motion Vector Height Attribution. *J. Meteorol. Clim.* **2009**, *48*, 450–463. [CrossRef]
15. Bormann, N.; Saarinen, S.; Kelly, G.; Thepaut, J.-N. The Spatial Structure of Observation Errors in Atmospheric Motion Vectors from Geostationary Satellite Data. *Mon. Weather Rev.* **2003**, *131*, 706–718. [CrossRef]
16. Genkova, I.; Borde, R.; Schmetz, J.; Daniels, J.; Velden, C.; Holmlund, K. Global atmospheric motion vector intercomparison study. In Proceedings of the 9th International Winds Workshop, Annapolis, MD, USA, 14–18 April 2008. Available online: https://www.researchgate.net/profile/Johannes-Schmetz/publication/237834561_GLOBAL_ATMOSPHERIC_MOTION_VECTOR_INTERCOMPARISON_STUDY/links/0c96052825b3d80e7f000000/GLOBAL-ATMOSPHERIC-MOTION-VECTOR-INTERCOMPARISON-STUDY.pdf (accessed on 1 November 2023).
17. Genkova, I.; Borde, R.; Schmetz, J.; Velden, C.; Holmlund, K.; Bormann, N.; Bauer, P. Global atmospheric motion vector intercomparison study. In Proceedings of the 10th International Winds Workshop, Tokyo, Japan, 22–26 February 2010. Available online: <https://cimss.ssec.wisc.edu/iwgg/iww10/talks/genkova2.pdf> (accessed on 1 November 2023).
18. Santek, D.; Hoover, B.; Zhang, H.; Moeller, C. Evaluation of Aeolus Winds by Comparing to AIRS 3D Winds, Rawinsondes, and Reanalysis Grids. In Proceedings of the 15th International Winds Workshop, Virtual, 12–16 April 2021; Available online: <https://www.ssec.wisc.edu/meetings/iwgg/2021-meeting/presentations/oral-santek/> (accessed on 9 May 2021).
19. Santek, D.; Dworak, R.; Wanzong, S.; Rink, T.; Lukens, K.; Reiner, S.; García-Pereda, J. *NWC SAF Winds Intercomparison Study Report: 2021*; International Winds Working Group, 2022. Available online: http://cimss.ssec.wisc.edu/iwgg/Docs/CIMSS_AMV_Comparison_2021_Report_02Nov2022.pdf (accessed on 1 November 2023).
20. Rani, S.I.; Jangid, B.P.; Kumar, S.; Bushair, M.T.; Sharma, P.; George, J.P.; George, G.; Das Gupta, M. Assessing the quality of novel Aeolus winds for NWP applications at NCMRWF. *Q. J. R. Meteorol. Soc.* **2022**, *148*, 1344–1367. [CrossRef]
21. Borde, R.; Hautecoeur, O.; Carranza, M. EUMETSAT global AVHRR wind product. *J. Atmos. Ocean. Technol.* **2016**, *33*, 429–438. [CrossRef]
22. Borde, R.; Carranza, M.; Hautecoeur, O.; Barbioux, K. Winds of change for future operational AMV at EUMETSAT. *Remote Sens.* **2019**, *11*, 2111. [CrossRef]
23. Martin, A.; Weissmann, M.; Reitebuch, O.; Rennie, M.; Geiß, A.; Cress, A. Validation of Aeolus winds using radiosonde observations and numerical weather prediction model equivalents. *Atmos. Meas. Tech.* **2021**, *14*, 2167–2183. [CrossRef]
24. Hoffman, R.N.; Lukens, K.E.; Ide, K.; Garrett, K. A collocation study of atmospheric motion vectors (AMVs) compared to Aeolus wind profiles with a feature track correction (FTC) observation operator. *Q. J. R. Meteorol. Soc.* **2022**, *148*, 321–337. [CrossRef]

25. Lukens, K.E.; Ide, K.; Garrett, K.; Liu, H.; Santek, D.; Hoover, B.; Hoffman, R.N. Exploiting Aeolus level-2b winds to better characterize atmospheric motion vector bias and uncertainty. *Atmos. Meas. Tech.* **2022**, *15*, 2719–2743. [[CrossRef](#)]
26. Lukens, K.E.; Ide, K.; Garrett, K. Investigation into the Potential Value of Stratospheric Balloon Winds Assimilated in NOAA's Finite-Volume Cubed-Sphere Global Forecast System (FV3GFS). *J. Geophys. Res. Atmos.* **2023**, *128*, e2022JD037526. [[CrossRef](#)]
27. Daniels, J.; NOAA/NESDIS/STAR, College Park, MD, USA. Personal communication, 2022.
28. Lukens, K.E.; Garrett, K.; Ide, K.; Santek, D.; Hoover, B.; Huber, D.; Hoffman, R.N.; Liu, H. System for Analysis of Wind Collocations (SAWC): A Novel Archive and Collocation Software Application for the Intercomparison of Winds from Multiple Observing Platforms User Manual. 2023. Available online: https://www.star.nesdis.noaa.gov/data/sawc/User_Manual/SAWC_User_Manual_v1.2.0.pdf (accessed on 22 September 2023).
29. Žagar, N.; Rennie, M.; Isaksen, L. Uncertainties in Kelvin Waves in ECMWF Analyses and Forecasts: Insights From Aeolus Observing System Experiments. *Geophys. Res. Lett.* **2021**, *48*, e2021GL094716. [[CrossRef](#)]
30. Bley, S.; Rennie, M.; Žagar, N.; Pinol Sole, M.; Straume, A.G.; Antifaev, J.; Candido, S.; Carver, R.; Fehr, T.; von Bismarck, J.; et al. Validation of the Aeolus L2B Rayleigh winds and ECMWF short-range forecasts in the upper troposphere and lower stratosphere using Loon super pressure balloon observations. *Q. J. R. Meteorol. Soc.* **2022**, *148*, 3852–3868. [[CrossRef](#)]
31. Tan, D.G.H.; Andersson, E.; de Kloe, J.; Marseille, G.; Stoffelen, A.; Poli, P.; Denneulin, M.; Dabas, A.; Huber, D.; Reitebuch, O.; et al. The ADM-Aeolus wind retrieval algorithms. *Tellus A* **2008**, *60*, 191–205. [[CrossRef](#)]
32. Rennie, M.; Tan, D.; Andersson, E.; Poli, P.; Dabas, A.; de Kloe, J.; Marseille, G.J. Aeolus Level-2B Algorithm Theoretical Basis Document (Mathematical Description of the Aeolus L2B Processor). Technical Report AED-SD-ECMWF-L2B-038, ECMWF. Version 3.40. 2020. Available online: <https://earth.esa.int/eogateway/documents/20142/37627/Aeolus-L2B-Algorithm-ATBD.pdf> (accessed on 28 February 2024).
33. Reitebuch, O.; Huber, D.; Nikolaus, I. ADM-Aeolus Algorithm Theoretical Basis Document ATBD Level1B Products. Technical Report, Aeolus 2018, REF: AE-RP-DLR-L1B-001. Available online: <https://earth.esa.int/eogateway/documents/20142/37627/Aeolus-L1B-Algorithm-ATBD.pdf> (accessed on 19 October 2023).
34. Reitebuch, O. The Spaceborne Wind Lidar Mission ADM-Aeolus. In *Atmospheric Physics*; Schumann, U., Ed.; Springer: Berlin, Germany, 2012; pp. 815–827. [[CrossRef](#)]
35. Straume, A.G.; Parrinello, T.; von Bismarck, J.; Bley, S.; Ehlers, F.; The Aeolus Teams. ESA's Wind Lidar Mission Aeolus—Status and scientific exploitation after 2.5 years in space. In Proceedings of the 15th International Winds Workshop, Virtual, 12–16 April 2021; Available online: https://www.ssec.wisc.edu/meetings/wp-content/uploads/sites/33/2021/02/IWW15_Presentation_AG_Straume.pdf (accessed on 9 May 2021).
36. Daniels, J.; Bresky, W.; Wanzong, S.; Velden, C.; Berger, H. NOAA/NESDIS/STAR GOES-R Advanced Baseline Imager (ABI) Algorithm Theoretical Basis Document For Derived Motion Winds, Version 2.5; NOAA NESDIS Center for Satellite Applications and Research: College Park, MD, USA, 2012. Available online: <https://www.star.nesdis.noaa.gov/goesr/docs/ATBD/DMW.pdf> (accessed on 19 July 2023).
37. Lux, O.; Witschas, B.; Geiß, A.; Lemmerz, C.; Weiler, F.; Marksteiner, U.; Rahm, S.; Schäfler, A.; Reitebuch, O. Quality control and error assessment of the Aeolus L2B wind results from the Joint Aeolus Tropical Atlantic Campaign. *Atmos. Meas. Tech.* **2022**, *15*, 6467–6488. [[CrossRef](#)]
38. Marseille, G.J.; de Kloe, J.; Marksteiner, U.; Reitebuch, O.; Rennie, M.; de Haan, S. NWP calibration applied to Aeolus Mie channel winds. *Q. J. R. Meteorol. Soc.* **2022**, *148*, 1020–1034. [[CrossRef](#)]
39. Dabas, A.; Denneulin, M.L.; Flamant, P.; Loth, C.; Garnier, A.; Dolfi-Bouteyre, A. Correcting Winds Measured with a Rayleigh Doppler Lidar from Pressure and Temperature Effects. *Tellus A* **2008**, *60*, 206–215. [[CrossRef](#)]
40. Rennie, M.P.; Isaksen, L.; Weiler, F.; de Kloe, J.; Kanitz, T.; Reitebuch, O. The impact of Aeolus wind retrievals on ECMWF global weather forecasts. *Q. J. R. Meteorol. Soc.* **2021**, *147*, 3555–3586. [[CrossRef](#)]
41. Weiler, F.; Rennie, M.; Kanitz, T.; Isaksen, L.; Checa, E.; de Kloe, J.; Reitebuch, O. Correction of wind bias for the lidar on-board Aeolus using telescope temperatures. *Atmos. Meas. Tech.* **2021**, *14*, 7167–7185. [[CrossRef](#)]
42. Weiler, F.; Kanitz, T.; Wernham, D.; Rennie, M.; Huber, D.; Schillinger, M.; Saint-Pe, O.; Bell, R.; Parrinello, T.; Reitebuch, O. Characterization of dark current signal measurements of the ACCDs used on board the Aeolus satellite. *Atmos. Meas. Tech.* **2021**, *14*, 5153–5177. [[CrossRef](#)]
43. Tritscher, I.; Pitts, M.C.; Poole, L.R.; Alexander, S.P.; Cairo, F.; Chipperfield, M.P.; Groöß, J.-U.; Höpfner, M.; Lambert, A.; Luo, B.; et al. Polar stratospheric clouds: Satellite observations, processes, and role in ozone depletion. *Rev. Geophys.* **2021**, *59*, e2020RG000702. [[CrossRef](#)]
44. Wilks, D. *Statistical Methods in the Atmospheric Sciences*, 4th ed.; Elsevier: Cambridge, MA, USA, 2019. [[CrossRef](#)]
45. James, E.P.; Benjamin, S.G.; Jamison, B.D. Commercial-aircraft-based observations for NWP: Global coverage, data impacts, and COVID-19. *J. Appl. Meteorol. Climatol.* **2020**, *59*, 1809–1825. [[CrossRef](#)]
46. Abdalla, S.; Flament, T.; Krisch, I.; Marksteiner, U.; Reitebuch, O.; Rennie, M.; Traçon, D.; Weiler, F. Verification Report of Second Reprocessing Campaign for FM-B from 24 June 2019 Till 9 October 2020. Technical Report, Aeolus Data Innovation Science Cluster DISC, Version 1.1, 2021, REF: AED-TN-ECMWF-GEN-060. Available online: <https://dragon3.esa.int/documents/d/earth-online/verification-report-of-the-second-reprocessing-campaign-for-fm-b> (accessed on 9 August 2023).

47. Zuo, H.; Hasager, C.B.; Karagali, I.; Stoffelen, A.; Marseille, G.J.; de Kloe, J. Evaluation of Aeolus L2B wind product with wind profiling radar measurements and numerical weather prediction model equivalents over Australia. *Atmos. Meas. Tech.* **2022**, *15*, 4107–4124. [[CrossRef](#)]
48. Lux, O.; Lemmerz, C.; Weiler, F.; Marksteiner, U.; Witschas, B.; Rahm, S.; Geiß, A.; Reitebuch, O. Intercomparison of wind observations from the European Space Agency’s Aeolus satellite mission and the ALADIN Airborne Demonstrator. *Atmos. Meas. Tech.* **2020**, *13*, 2075–2097. [[CrossRef](#)]
49. Reitebuch, O.; Lemmerz, C.; Lux, O.; Marksteiner, U.; Rahm, S.; Weiler, F.; Witschas, B.; Meringer, M.; Schmidt, K.; Huber, D.; et al. Initial Assessment of the Performance of the First Wind Lidar in Space on Aeolus. In Proceedings of the 29th International Laser Radar Conference (ILRC 29), EPJ Web of Conferences, Hefei, China, 24–28 June 2019; Volume 237, pp. 1–4. [[CrossRef](#)]
50. Bormann, N.; Kelly, G.; Thépaut, J.-N. Characterising and correcting speed biases in atmospheric motion vectors within the ECMWF system. In Proceedings of the 6th International Winds Workshop, Madison, WI, USA, 7–10 May 2002. Available online: http://cimss.ssec.wisc.edu/iwvw/iwvw6/session3/bormann_1_bias.pdf (accessed on 18 April 2021).
51. Cordoba, M.; Dance, S.L.; Kelly, G.A.; Nichols, N.K.; Walker, J.A. Diagnosing atmospheric motion vector observation errors for an operational high-resolution data assimilation system. *Q. J. R. Meteor. Soc.* **2017**, *143*, 333–341. [[CrossRef](#)]
52. Posselt, D.; Wu, L.; Mueller, K.; Huang, L.; Irion, F.W.; Brown, S.; Su, H.; Santek, D.; Velden, C.S. Quantitative Assessment of State-Dependent Atmospheric Motion Vector Uncertainties. *J. Appl. Meteorol. Clim.* **2019**, *58*, 2479–2495. [[CrossRef](#)]
53. Quaas, J.; Gryspeerdt, E.; Vautard, R.; Boucher, O. Climate impact of aircraft-induced cirrus assessed from satellite observations before and during COVID-19. *Environ. Res. Lett.* **2021**, *16*, 064051. [[CrossRef](#)]
54. Reifenberg, S.F.; Martin, A.; Kohl, M.; Bacer, S.; Hamryszczak, Z.; Tadic, I.; Röder, L.; Crowley, D.J.; Fischer, H.; Kaiser, K.; et al. Numerical simulation of the impact of COVID-19 lockdown on tropospheric composition and aerosol radiative forcing in Europe. *Atmos. Chem. Phys.* **2022**, *22*, 10901–10917. [[CrossRef](#)]
55. Clark, H.; Bennouna, Y.; Tsvilidou, M.; Wolff, P.; Sauvage, B.; Barret, B.; Le Flochmoën, E.; Blot, R.; Boulanger, D.; Cousin, J.-M.; et al. The effects of the COVID-19 lockdowns on the composition of the troposphere as seen by In-service Aircraft for a Global Observing System (IAGOS) at Frankfurt. *Atmos. Chem. Phys.* **2021**, *21*, 16237–16256. [[CrossRef](#)]
56. Chen, Y. COVID-19 pandemic imperils weather forecast. *Geophys. Res. Lett.* **2020**, *47*, e2020GL088613. [[CrossRef](#)] [[PubMed](#)]
57. Rani, S.I.; Jangid, B.P.; Francis, T.; Sharma, P.; George, G.; Kumar, S.; Thota, M.S.; George, J.P.; Nath, S.; Gupta, M.D.; et al. Assimilation of aircraft observations over the Indian monsoon region: Investigation of the effects of COVID-19 on a reanalysis. *Q. J. R. Meteor. Soc.* **2023**, *149*, 894–910. [[CrossRef](#)]
58. Moninger, W.R.; Benjamin, S.G.; Jamison, B.D.; Schlatter, T.W.; Smith, T.L.; Szoke, E.J. Evaluation of regional aircraft observations using TAMDAR. *Weather. Forecast.* **2010**, *25*, 627–645. [[CrossRef](#)]
59. Petersen, R.A. On the impact and benefits of AMDAR observations in operational forecasting Part I: A Review of the Impact of Automated Aircraft Wind and Temperature Reports. *BAMS* **2016**, *97*, 585–602. [[CrossRef](#)]
60. Boukabara, S.A.; Zhu, T.; Tolman, H.L.; Lord, S.; Goodman, S.; Atlas, R.; Goldberg, M.; Auligne, T.; Pierce, B.; Cucurull, L.; et al. S4: An O2R/R2O infrastructure for optimizing satellite data utilization in NOAA numerical modeling systems. A step toward bridging the gap between research and operations. *BAMS* **2016**, *97*, 2359–2378. [[CrossRef](#)]

Disclaimer/Publisher’s Note: The statements, opinions and data contained in all publications are solely those of the individual author(s) and contributor(s) and not of MDPI and/or the editor(s). MDPI and/or the editor(s) disclaim responsibility for any injury to people or property resulting from any ideas, methods, instructions or products referred to in the content.